Biomedicine & Pharmacotherapy 174 (2024) 116496

Contents lists available at ScienceDirect

Biomedicine & Pharmacotherapy

journal homepage: www.elsevier.com/locate/biopha

Novel hybrid compounds of sclareol and doxorubicin as potential anticancer nanotherapy for glioblastoma

Ana Stepanović [a], Nataša Terzić Jovanović [b], Aleksandra Korać [c], Mario Zlatović [d], Igor Nikolić [e,f], Igor Opsenica [d], Milica Pešić [a,*]

[a] Institute for Biological Research "Siniša Stanković" - National Institute of the Republic of Serbia, University of Belgrade, Despota Stefana 142, Belgrade 11108, Serbia
[b] University of Belgrade – Institute of Chemistry, Technology and Metallurgy – National Institute of the Republic of Serbia, Njegoševa 12, Belgrade 11000, Serbia
[c] University of Belgrade – Faculty of Biology & Center for Electron Microscopy, Studentski trg 16, Belgrade 11158, Serbia
[d] University of Belgrade – Faculty of Chemistry, Studentski trg 12-16, Belgrade 11158, Serbia
[e] Clinic for Neurosurgery, Clinical Center of Serbia, Pasterova 2, Belgrade 11000, Serbia
[f] School of Medicine, University of Belgrade, Doktora Subotića 8v, Belgrade 11000, Serbia

ARTICLE INFO

Keywords:
hybrid compounds
sclareol, doxorubicin
glioblastoma
cancer multidrug resistance
nanoparticles

ABSTRACT

Two novel hybrid compounds, CON1 and CON2, have been developed by combining sclareol (SC) and doxorubicin (DOX) into a single molecular entity. These hybrid compounds have a 1:1 molar ratio of covalently linked SC and DOX. They have demonstrated promising anticancer properties, especially in glioblastoma cells, and have also shown potential in treating multidrug-resistant (MDR) cancer cells that express the P-glycoprotein (P-gp) membrane transporter. CON1 and CON2 form nanoparticles, as confirmed by Zetasizer, transmission electron microscopy (TEM), and chemical modeling. TEM also showed that CON1 and CON2 can be found in glioblastoma cells, specifically in the cytoplasm, different organelles, nucleus, and nucleolus. To examine the anticancer properties, the U87 glioblastoma cell line, and its corresponding multidrug-resistant U87-TxR cell line, as well as patient-derived astrocytoma grade 3 cells (ASC), were used, while normal human lung fibroblasts were used to determine the selectivity. CON1 and CON2 exhibited better resistance and selectivity profiles than DOX, showing less cytotoxicity, as evidenced by real-time cell analysis, DNA damage determination, cell death induction, mitochondrial respiration, and mitochondrial membrane depolarization studies. Cell cycle analysis and the β-galactosidase activity assay suggested that glioblastoma cells die by senescence following CON1 treatment. Overall, CON1 and CON2 showed great potential as they have better anticancer features than DOX. They are promising candidates for additional preclinical and clinical studies on glioblastoma.

1. Introduction

Nature has always been a source of inspiration for disease treatment. Most of the approved medicines have been either isolated from natural sources or developed from compounds found in nature. In this era of persistent pursuit of answers to one of the deadliest diseases in the world, cancer, it is crucial to explore novel approaches with natural compounds to overcome this challenge.

Sclareol (SC) is a natural compound found in the clary sage plant (*Salvia sclarea* L.), known for its wide range of health benefits. With its anti-inflammatory, antimicrobial, antidiabetic, and antihypertensive properties, it is a safe and effective option for medicinal use [1]. When taken orally, it has shown no adverse effects and is well-tolerated [2]. Moreover, SC has demonstrated significant potential as an anticancer

---

Abbreviations: ABC, ATP Binding Cassette; ASC, WHO grade 3 anaplastic astrocytoma; AV, Annexin-V-FITC; BBB, blood-brain barrier; CI, combination index; CON1 and CON2, novel hybrid compounds; DHE, dihydroethidium; DHR, dihydrorhodamine 123; DMEM, Dulbecco's modified minimal essential medium; DOX, doxorubicin; DMSO, dimethyl sulfoxide; FBS, fetal bovine serum; FDG, fluorescein-di-D-galacto-pyranoside; GFAP, Glial Fibrillary Acidic Protein; LIG1 and LIG2, sclareol derivatives; MAP2, Microtubule Associated Protein 2; MDR, multidrug-resistant; MEM, minimal essential medium; MRI, magnetic resonance imaging; MTT, 3-[4,5-dimethylthiazol-2-yl]-2,5-diphenyltetrazolium bromide; NSCLC, non-small cell lung carcinoma; OCR, oxygen consumption rate; OLIG2, Oligodendrocyte transcription factor 2; P53, tumor protein P53; P-gp, P-glycoprotein; PDI, polydispersity index; PI, propidium iodide; RNS, reactive nitrogen species; ROS, reactive oxygen species, SC, sclareol; TEM, transmission electron microscopy; TMZ, temozolomide.

* Corresponding author.
E-mail address: camala@ibiss.bg.ac.rs (M. Pešić).

https://doi.org/10.1016/j.biopha.2024.116496
Received 14 December 2023; Received in revised form 11 March 2024; Accepted 20 March 2024

agent in various *in vitro* studies. It has been found to induce apoptosis and inhibit proliferation in several cancer cell lines, including leukemic, colon, osteosarcoma, and cervical cancer cells [3–7]. The therapeutic effects of SC in xenograft model of small cell lung cancer cells also showed promising results [8]. Additionally, SC is capable of crossing the blood-brain barrier (BBB) [9] and modulate the activity of P-glycoprotein (P-gp) [10], which belongs to the ATP Binding Cassette (ABC) transporters involved in drug transport across biological barriers [11].

Doxorubicin (DOX) is a powerful antitumor agent commonly used as a first-line treatment for various types of cancer. Its source is the bacterium *Streptomyces peucetius*, and it operates by intercalating into DNA, hindering DNA synthesis, and promoting cell death. Additionally, DOX creates reactive oxygen species (ROS) that result in DNA damage and induce apoptosis [12]. Nevertheless, DOX faces multiple drawbacks as a clinical treatment due to its lack of tumor specificity and severe side effects, such as myelosuppression, nephrotoxicity, dose-dependent cardiotoxicity, and development of multidrug resistance (MDR) caused by P-gp [13,14]. Among these, cardiotoxicity is an especially serious side effect that can lead to myocardial damage, arrhythmias, and even heart failure [15]. This condition arises when DOX generates toxic intermediates and ROS that cause cardiomyocyte apoptosis [16]. To surmount DOX's limitations, researchers are exploring alternative treatments that are more potent and less harmful.

Glioblastoma is a type of brain tumor that is known for its high invasiveness, poor prognosis, high mortality rate, and frequent recurrence. It is the most common and aggressive brain tumor, accounting for almost 48% of diagnosed cases [17]. Unfortunately, the incidence of recurrence is very high, making the median overall survival just 14 months and the 5-year survival rate less than 7% [18]. It's important to note that temozolomide (and bevacizumab in special occasions) is the only approved chemotherapeutic agent for glioblastoma therapy [19,20]. However, no new chemotherapy has been approved for glioblastoma treatment since 2005, which is a significant challenge. Limited efficacy of chemotherapy for glioblastoma is primarily due to the inadequate delivery of most therapeutics across the BBB and the evolution of MDR, which are all mediated by P-gp [21].

Researchers are exploring ways to improve the efficacy of DOX in cancer treatment while reducing its adverse effects and resistance to therapy. Nanoparticle-based formulations have been investigated as an ideal drug delivery system for chemotherapeutic agents. Although there have been attempts to use DOX in nanoparticle formulations for glioblastoma, they have been unsuccessful [22]. However, a promising example was the use of poly lactic-co-glycolic acid nanoparticles coated with poloxamer 188 to deliver DOX, which has been shown to significantly inhibit tumor growth and prolong survival in rats with intracranial glioblastoma [23]. Despite challenges such as low encapsulation rate, complicated preparation processes, and poor stability for long-term storage [13], the potential benefits of nanoparticle-based drug delivery systems for cancer treatment make further research and development worthwhile.

Numerous clinical trials have been conducted to investigate methods of improving DOX delivery to glioblastoma. The efficacy of pegylated liposomal DOX and prolonged administration of TMZ in addition to radiotherapy for newly diagnosed glioblastoma was investigated [24]. While the combination was found to be tolerable, it did not result in significant improvement in patient outcomes compared to existing data. An EnGeneIC delivery vehicle (EDV) that delivers chemotherapeutic drugs was used for DOX treatment [25]. The study revealed that (V) EDVDox, a treatment targeting EGFR via Vectibix and containing DOX within EDV, is a promising option. The study established a safe maximum tolerated dose and recommended Phase II. Additionally, anti-EGFR immunoliposomes loaded with DOX were found to effectively deliver the drug to glioblastoma [26]. The liposomes could not cross the BBB but effectively delivered DOX to glioblastoma tissue with compromised BBB. No new safety issues were observed. However, the median progression-free survival was 1.5 months, while the median overall survival was eight months. A recent pilot study will be conducted on pediatric patients who will receive treatment with DOX [27]. This study will use advanced magnetic resonance imaging (MRI) techniques and serum biomarkers to measure the duration of maximum BBB disruption, which is a suitable period for treatment with DOX. This study was based on an earlier clinical trial investigation in which MRI-guided laser therapy was applied to patients with recurrent glioblastoma, resulting in disruption of the BBB [28]. The disruption peaked within 1–2 weeks after treatment and resolved by 4–6 weeks, providing a window of opportunity to enhance the delivery of DOX that is blocked by the BBB. Serum levels of brain-specific enolase were used to independently quantify BBB disruption. The study is expected to be completed by 2030.

Current clinical trial uses a novel device equipped with nine ultrasound emitters that can temporarily and reversibly open the BBB to improve the penetration of drugs into the brain [29]. Immunotherapeutics and liposomal DOX will be investigated in conjunction with a novel device. The study is expected to be completed by 2026.

Overall, these studies demonstrate a concerted effort to find more efficient treatments for glioblastoma using DOX, despite the challenges posed by the BBB.

Combining drugs with different mechanisms of action can lead to a synergistic effect, which can enhance therapeutic efficacy. Interestingly, there are only four published papers on the combination of SC and DOX with possible anticancer activity. However, these papers reveal a promising potential for this combination in cancer treatment. For instance, one study showed that SC significantly enhanced the cytotoxic effect of DOX on breast cancer cell lines, leading to a significant inhibition of cell growth [30]. Another study indicated that SC increased DOX cytotoxicity 4.5-fold in spheroids of a DOX-resistant ovarian cancer cell line [31]. Additionally, combining DOX and SC in a nanolipid carrier achieved a better synergistic antitumor effect on breast cancer cell lines than using either drug alone [32,33]. Most importantly, this combination did not cause side effects in animals.

Considering the safety of SC for human use and its ability to cross the BBB and inhibit P-gp activity, which can impede the efficacy of DOX in cancer treatment, the advantages of hybrid structures based on natural products and/or drugs, and the literature data that points to SC's ability to potentiate DOX effects in some types of tumors, it is worth exploring the potential of combining these two drugs as a single molecule, hybrid compound, to develop more effective cancer therapies. This study presents a comprehensive characterization of two hybrid compounds synthesized through a convergent process by combining SC and DOX [34]. The primary objective of our research was to analyze the physico-chemical properties of these compounds, including their nanoparticle nature, and their intracellular localization. In addition, we investigated the potential anticancer effects of these compounds in glioblastoma cells. By providing an in-depth analysis of the properties and effects of these hybrid compounds, we hope to contribute to the preclinical studies and development of more effective therapies for glioblastoma.

2. Material and methods

2.1. Synthesis of SC derivatives, LIG1, LIG2, and SC:DOX hybrid compounds CON1 and CON2

2.1.1. Examples

The following examples illustrate the synthesis of some compounds of the invention. These examples are not limiting and are provided for illustrative purposes.

Melting points were determined using a Boetius PMHK apparatus and were not corrected. IR spectra were recorded on a Thermo-Scientific Nicolet 6700 FT-IR "diamond crystal" spectrophotometer. Absorption band positions are expressed in cm-1. ^{1}H NMR and ^{13}C NMR spectra were recorded on a Varian spectrometer (at 400 and 100 MHz) in the specified solvent. Chemical shifts are expressed in ppm, coupling constants (J) in Hz, and signal multiplicity is indicated as s (singlet), d (doublet), t (triplet), q (quartet), sext (sextet), dd (doublet of doublets), dq (doublet of quartets), and m (multiplet). HRMS-HESI spectra were recorded on an LTQ Orbitrap XL (Thermo Fisher Scientific Inc., USA) mass spectrometer. Samples were dissolved in pure HPLC-grade ACN and directly injected into the instrument. Ionization was performed in positive mode on a heated electrospray ionization probe. The following HESI parameters were used: spray voltage 4.7 kV, evaporation temperature 60 °C, drying gas and auxiliary gas flow rates of 24 and 10 (arbitrary units), respectively, capillary voltage 49 V, capillary temperature 275 °C, tube lens voltage 80 V, resolution (for m/z 400): 30,000. For thin-layer chromatography, SiO_2 and RP-18 plates (Merck) were used. SiO_2 (0.018–0.032 mm) was used for "dry-flash" chromatography.

Complete structural characterization of the synthesized compounds was achieved by determining melting points and employing infrared spectroscopy (IC ATR), nuclear magnetic resonance (1D NMR (1 H and 13 C) methods and 2D NMR (COSY (1–1 H Correlation Spectroscopy), NOESY (Nuclear Overhauser Effect Spectroscopy), HSQC (1 H-13 C Heteronuclear Single Quantum Coherence), HMBC (1 H-13 C Heteronuclear Multiple Bond Correlation)) methods), as well as high-resolution mass spectrometry (HRMS).

The purity (HPLC) of the compounds was determined using an Agilent 1200 HPLC system equipped with a Quat Pump (G1311B), Injector (G1329B, 1260 ALS, TCC 1260 (G1316A), and Detector 1260 DAD VL+ (G1315C)). HPLC analyses were performed in two different systems.

Method A: InfinityLab Poroshell 120 CS-C18 4.6 × 100 mm 2.7μ, S. N. was used as the stationary phase. The eluent consisted of the following solvents: 0.1% HCOOH in water (A) and MeOH (B). Analyses were performed at the UV maximum of the compound (254 nm) to achieve maximum selectivity. Compounds were dissolved in MeOH at final concentrations of approximately 1 mg/mL, and the injection volume was 5 μL. The flow rate was 0.6 mL/min. Compounds LIG1, LIG2, CON1, and CON2 were eluted using the following gradient: 0 – 1 min 95% A, 1– 6 min 95% A → 5% A, 6–11 min 5% A, 11 – 14 min 5% A → 95% A, 14–15 min 95% A.

Method B: InfinityLab Poroshell 120 CS-C18, 4.6 × 100 mm, 2.7μm, with Serial Number (S.N.), was employed as the stationary phase. The eluent consisted of the following solvents: 0.1% HCOOH in water (A) and acetonitrile (ACN) (B). Analyses were conducted at the UV maximum of the compound (254 nm) to achieve maximum selectivity. Compounds were dissolved in methanol (MeOH) at final concentrations of approximately 1 mg/mL, and the injection volume was set at 5 μL. The flow rate was maintained at 0.6 mL/min. Compounds LIG1, LIG2, CON1, and CON2 were eluted using the following gradient: 0 – 1 min, 95% A; 1– 6 min, 95% A → 5% A; 6–11 min, 5% A; 11 – 14 min, 5% A → 95% A; 14–15 min, 95% A.

The applied experimental conditions did not impact the stereoisomerism of chiral carbon atoms within the sclareol subunit and doxorubicin.

2.1.1.1. Example of the synthesis of derivative 1 of sclareol: 4-{(1E,3 R)-3-hydroxy-5-[(2 R,4aS,8aS)-2-hydroxy-2,5,5,8a-tetramethyldecahydronaphthalen-1-yl]-3-methylpent-1-en-1-yl}benzaldehyde. In an oxygen-free environment, dimethylformamide (DMF) (1.5 mL), sclareol SC (30 mg, 0.097 mmol, 1 equiv), 4-formylphenylboronic acid (22 mg, 0.146 mmol, 1.5 equiv), $Pd(OAc)_2$ (2.2 mg, 0.010 mmol, 0.1 equiv), $Cu(OAc)_2$ (35.3 mg, 0.194 mmol, 2.0 equiv), and NaOAc (23.9 mg, 0.292 mmol, 3 equiv) were added to a round-bottom flask. The reaction mixture was stirred at 80 °C for 2 h. The reaction mixture was then filtered through a sintered funnel, washed with 3 × 20 mL of ethyl acetate (EtOAc), and dried over anhydrous $MgSO_4$. Compound 1 was obtained after dry-flash column chromatography (SiO_2: Hex/EtOAc = 7/3) as a yellow oil (32 mg, 80%). ^1H NMR (400 MHz, $CDCl_3$): δ = 9.97 (s, 1 H, -CHO), 7.81 (d, J = 7.9 Hz, 2 H, 2 × Ar-H), 7.50 (d, J = 7.9 Hz, 2 H, 2 × Ar-H), 6.69 (d, J = 16.0 Hz, 1 H, =CH), 6.46 (d, J = 16.2 Hz, 1 H, =CH), 2.45 (brs, 2 H, 2 × OH), 1.84 (d, J = 12.1 Hz, 1 H), 1.80 – 1.72 (m, 2 H), 1.68 – 1.53 (m, 4 H), 1.47 – 1.39 (m, 3 H), 1.38 (s, 3 H), 1.37 – 1.33 (m, 1 H), 1.29 – 1.25 (m, 1 H), 1.24 – 1.21 (m, 1 H), 1.17 (s, 3 H, Me), 1.15 – 1.07 (m, 1 H), 1.02 – 0.88 (m, 2 H), 0.85 (s, 3 H, Me), 0.78 (s, 6 H, 2 × Me) ppm. ^{13}C NMR (100 MHz, $CDCl_3$): δ = 191.9, 143.7, 142.0, 135.3, 130.3, 127.0, 125.7, 75.2, 73.7, 61.4, 56.2, 45.1, 44.6, 42.1, 39.9, 39.4, 33.5, 33.4, 27.6, 24.5, 21.6, 20.6, 19.2, 18.5, 15.4 ppm. HRMS (HESI/Orbitrap) m/z: $[M + Na]^+$ Calcd for $C_{27}H_{41}O_3Na^+$ 435.28697; Found 435.28704. IR (ATR): ν = 3379, 2927, 2868, 2735, 1698, 1601, 1568, 1461, 1388, 1306, 1266, 1214, 1167, 1133, 1099, 1085, 1065, 1039, 997, 972, 938, 908, 863, 812, 786, 737, 702, 661 cm^{-1}. $[\alpha]_D^{25}$ + 36.2 (c = 0.21 g/mol, MeOH).

2.1.1.2. Example of the synthesis of compound 2: 4-[(6-aminopropyl) amino]-4-oxobutanoic acid. A solution of succinic anhydride (271 mg, 2.70 mmol) in tetrahydrofuran (THF) (5 mL) was slowly added over 1 hour to a solution of 1,3-diaminopropane (200 mg, 2.70 mmol) in THF (10 mL). The reaction mixture was stirred at room temperature for 2 h. The reaction was quenched, and the solvent was removed under reduced pressure to yield the crude product. Compound 2 was obtained after dry-flash column chromatography (SiO_2: DCM → DCM/MeOH 1/1 → MeOH) as a colorless solid (376 mg, 80%). ^1H NMR (400 MHz, D_2O) δ = 3.15 (t, J = 6.6 Hz, 2 H, $-CH_2NHCO-$), 2.91 – 2.82 (m, 2 H, $-CH_2NH_2$), 2.32 (s, 4 H, $-CH_2COOH$ and $-CH_2CONH$), 1.78 – 1.67 (m, 2 H, $-CH_2CH_2NH_2$) ppm.^{13}C NMR (101 MHz, D_2O) δ = 180.82, 176.34, 36.84, 35.78, 32.82, 32.15, 26.61 ppm.

2.1.1.3. Example of the synthesis of compound 3: 4-[(6-aminohexyl) amino]-4-oxobutanoic acid. In a solution of succinic anhydride (200 mg, 2.00 mmol) in tetrahydrofuran (THF) (5 mL), a solution of 1,6-diaminohexane (232 mg, 2.00 mmol) in THF (10 mL) was slowly added over 1 hour. The reaction mixture was stirred at room temperature for 2 h. The reaction was terminated, and the solvent was removed under reduced pressure to obtain the crude product. Compound 3 was obtained after dry-flash column chromatography (SiO_2: DCM → DCM/MeOH 1/1 → MeOH) as a colorless solid substance (290 mg, 78%). ^1H NMR (400 MHz, D_2O) δ = 3.19 (t, J = 6.7 Hz, 2 H, $-CH_2NHCO-$), 3.01 (d, J = 7.5 Hz, 2 H, $-CH_2NH_2$), 2.46 (s, 4 H, $-CH_2COOH$ and $-CH_2CONH$), 1.73 – 1.62 (m, 2 H, $-CH_2CH_2NH_2$), 1.57 – 1.47 (m, 2 H, $-CH_2CH_2NHCO-$), 1.46 – 1.36 (m, 4 H, $-CH_2CH_2CH_2NH_2$ and $-CH_2CH_2CH_2CH_2NH_2$) ppm. ^{13}C NMR (101 MHz, D_2O) δ = 180.80, 175.64, 39.29, 38.95, 33.05, 32.38, 27.89, 26.47, 25.21, 24.99 ppm.

2.1.2. Synthesis of Ligand LIG1: 4-((3-((4-((R,E)-3-hydroxy-5-((1 R,2 R,4aS,8aS)-2-hydroxy-2,5,5,8a-tetramethyldecahydronaphthalen-1-yl)-3-methylpent-1-en-1-yl)benzyl)amino)propyl)amino)-4-oxobutanoic acid

In a flame-dried round-bottom flask, dry MeOH (4 mL) was added, followed by 4-{(1E,3 R)-3-hydroxy-5-[(2 R,4aS,8aS)-2-hydroxy-2,5,5,8a-tetramethyldecahydronaphthalen-1-yl]-3-methylpent-1-en-1-yl}benzaldehyde 1 (80 mg, 0.194 mmol) and $Ti(Oi\text{-}Pr)_4$ (235 μL, 0.776 mmol). Then, a solution of amine 2 (101 mg, 0.586 mmol) in dry MeOH (0.5 mL) was slowly added. The reaction mixture was left stirring at room temperature overnight, after which $NaBH_4$ (13 mg, 0.388 mmol) was added to the solution, and the reaction mixture was further stirred for 2 h at room temperature. The reaction was quenched by adding water (3 mL), and the reaction mixture was filtered through a silica gel column, followed by thorough washing with DCM. Removal of the solvent under reduced pressure yielded the crude product. Compound LIG1 was obtained after dry-flash column chromatography (SiO_2: DCM→DCM/MeOH (NH_3) = 8/2) as a colorless solid (94 mg, 85%) with a melting point of 108–110 °C. ^1H NMR (400 MHz, CD_3OD): δ = 7.43 (d, J = 8.2 Hz, 2 H, 2 × Ar-H), 7.37 (d, J = 8.3 Hz, 2 H, 2 × Ar-H), 6.60 (d, J = 16.1 Hz, 1 H, =CH), 6.36 (d, J = 16.2 Hz, 1 H, =CH), 3.88 (s, 2 H, $Ar\text{-}CH_2\text{-}N$), 3.26 (t, J = 6.5 Hz, 2 H, $-CH_2NHCO-$), 2.80 (t, J = 7.2 Hz, 2 H, $-CH_2NHCH_2Ar-$), 2.46 – 2.35 (m, 4 H, $-CH_2COOH$ and $-CH_2CONH$), 1.88 – 1.79 (m, 2 H), 1.78 – 1.73 (m, 2 H), 1.72 – 1.60 (m, 4 H), 1.60 – 1.50 (m, 1 H), 1.49 – 1.37 (m, 4 H), 1.36 (s, 3 H, Me), 1.36 – 1.28 (m, 1 H), 1.25 – 1.15 (m, 1 H), 1.15 – 1.12 (m, 1 H), 1.12 (s, 3 H, Me), 1.03 – 0.93 (m, 2 H), 0.89 (s, 3 H, Me), 0.83 (s, 3 H, Me), 0.82 (s, 3 H, Me) ppm. ^{13}C NMR (101 MHz, CD_3OD): δ = 180.67, 176.74, 164.67, 162.52, 138.83, 130.37, 127.65, 127.57, 75.17, 74.35, 62.73, 57.56, 53.45, 49.85, 49.28, 47.08, 46.56, 45.17, 43.25, 41.18, 40.56, 37.44, 34.64, 34.18, 33.90, 33.88, 29.19, 27.82, 23.97, 21.95, 21.54, 20.84, 19.50, 16.05 ppm. HRMS (HESI/Orbitrap) m/z: $[M + H]^+$ Calcd for $C_{34}H_{55}O_5N_2$ 571.41055; Found 571.41120. IR (ATR): ν = 3292, 2929, 2867, 1640, 1562, 1459, 1388, 1301, 1270, 1219, 1188, 1157, 1132, 1085, 1033, 996, 970, 938, 908, 865, 640 cm^{-1}. HPLC purity, method E: t_R = 7.608 min, area 99.42%. Method B: t_R = 6.137 min, area 99.07% (λ = 254 nm). $[\alpha]_D^{25}$ + 0.054 (c = 3.3 $\times 10^{-3}$ g/mol, MeOH).

2.1.3. Synthesis of ligand LIG2: 4-((6-((4-((R,E)-3-hydroxy-5-((1 R,2 R,4aS,8aS)-2-hydroxy-2,5,5,8a-tetramethyldecahydronaphthalen-1-yl)-3-methylpent-1-en-1-yl)benzyl)amino)hexyl)amino)-4-oxobutanoic acid

In a flame-dried round-bottom flask, dry MeOH (4 mL) was added, followed by 4-{(1E,3 R)-3-hydroxy-5-[(2 R,4aS,8aS)-2-hydroxy-2,5,5,8a-tetramethyldecahydronaphthalen-1-yl]-3-methylpent-1-en-1-yl}benzaldehyde 1 (95 mg, 0.231 mmol) and Ti(O*i*-Pr)$_4$ (262 µL, 0.924 mmol). Then, a solution of amine 3 (150 mg, 0.694 mmol) in dry MeOH (0.5 mL) was slowly added. The reaction mixture was left stirring at room temperature overnight, after which $NaBH_4$ (17.4 mg, 0.462 mmol) was added to the solution, and the reaction mixture was further stirred for 2 h at room temperature. The reaction was quenched by adding water (3 mL), and the reaction mixture was filtered through a silica gel column, followed by thorough washing with DCM. Removal of the solvent under reduced pressure yielded the crude product. Compound LIG2 was obtained after dry-flash chromatography (SiO_2: DCM→DCM/MeOH(NH_3) = 8/2) as a colorless solid (141 mg, 83%) with a melting point of 124–126 °C. ^{1}H NMR (400 MHz, CD_3OD): δ = 7.49 (d, *J* = 8.1 Hz, 2 H, 2 × Ar-H), 7.44 (d, *J* = 8.2 Hz, 2 H, 2 × Ar-H), 6.61 (d, *J* = 16.1 Hz, 1 H, =CH), 6.41 (d, *J* = 16.1 Hz, 1 H, =CH), 4.14 (s, 2 H, Ar-CH_2-N), 3.19 (t, *J* = 6.3 Hz, 2 H, -CH_2NHCO-), 2.99 (t, *J* = 7.7 Hz, 2 H, -CH_2NHCH_2Ar-), 2.50 – 2.35 (m, 4 H, -CH_2COOH and -CH_2CONH), 1.93 – 1.77 (m, 2 H), 1.75 – 1.56 (m, 6 H), 1.55 – 1.46 (m, 3 H), 1.44 – 1.37 (m, 6 H), 1.35 (s, 3 H, Me), 1.35 – 1.28 (m, 1 H), 1.22 – 1.16 (m, 1 H), 1.15 – 1.10 (m, 1 H), 1.11 (s, 3 H, Me), 1.00 – 0.91 (m, 2 H), 0.88 (s, 3 H, Me), 0.82 (s, 3 H, Me), 0.81 (s, 3 H, Me) ppm. ^{13}C NMR (101 MHz, CD_3OD): δ = 180.53, 176.00, 140.04, 139.84, 132.01, 131.16, 127.95, 127.20, 75.17, 74.35, 62.73, 57.56, 54.80, 52.08, 49.29, 48.18, 47.03, 45.17, 43.25, 41.17, 40.55, 39.75, 34.61, 34.18, 33.94, 33.90, 29.84, 27.92, 27.06, 26.83, 26.69, 23.95, 21.94, 21.53, 20.82, 19.51, 16.05 ppm. HRMS (HESI/Orbitrap) m/z: $[M + H]^+$ Calcd for $C_{37}H_{61}O_5N_2$ 613.45750; Found 613.45804. IR (ATR): ν = 3289, 3089, 2927, 2862, 1635, 1561, 1437, 1387, 1300, 1268, 1216, 1178, 1132, 1084, 1032, 995, 970, 938, 908, 864, 802, 724, 642, 563 cm^{-1}. HPLC purity, method A: t_R = 7.683 min, area 99.32%. Method B: t_R = 6.191 min, area 99.11% (λ = 254 nm). $[\alpha]_D^{25}$ + 0.054 (c = 1.3 $\times 10^{-3}$ g/mol, MeOH).

2.1.4. Synthesis of CON1: N1-((2 S,3 S,4 S,6 R)-3-hydroxy-2-methyl-6-(((1 S,3 S)-3,5,12-trihydroxy-3-(2-hydroxyacetyl)-10-methoxy-6,11-dioxo-1,2,3,4,6,11-hexahydrotetracen-1-yl)oxy)tetrahydro-2 H-pyran-4-yl)-N4-(3-((4-((R,E)-3-hydroxy-5-((1 R,2 R,4aS,8aS)-2-hydroxy-2,5,5,8a-tetramethyldecahydronaphthalen-1-yl)-3-methylpent-1-en-1-yl)benzyl)amino)propyl)succinamide

In a solution of doxorubicin hydrochloride (21 mg, 0.036 mmol) in dry DMF (500 µL), diisopropylethylamine (6 µL, 0.050 mmol) was added. The addition of DIEA caused the solution to change color from light red to dark red. The reaction mixture was left stirring at room temperature for 30 minutes under argon, followed by the addition of compound LIG1 (21 mg, 0.036 mmol). After cooling the reaction mixture in an ice bath (0 °C), solutions of HOBT (6.1 mg, 0.050 mmol) and EDCI (9.4 mg, 0.050 mmol) in dry DMF (100 µL each) were added sequentially. The reaction mixture was stirred for 30 minutes at 0 °C and then for 18 h at room temperature in the dark. The reaction progress was monitored using an Agilent 1200 HPLC system equipped with a reverse-phase analytical InfinityLab Poroshell 120 CS-C18 column (4.6 × 100 mm, 2.7µ, S.N. USKBM01053). The mobile phase consisted of a mixture of 0.1% aqueous formic acid and ACN with a programmed isocratic and gradient elution: 0–1 min, 5% ACN; 1–6 min, 5%→95% ACN; 6–12 min, 95% ACN; 12–14 min, 95% A→5% ACN; 14–15 min, 5% ACN. The flow rate was 0.6 mL/min. Signal detection was performed in the wavelength range of 254/280 nm using a DAD detector. After 12 h, the reaction was stopped, and the reaction mixture was concentrated under reduced pressure. The crude reaction mixture was purified on an HPLC-DAD system using a semi-preparative ZORBAX Eclipse XDB-C18 column (9.4 × 250 mm, 5µ, S.N. USSY004729) (DAD detector: 254 nm). The mobile phase consisted of a mixture of 0.1% aqueous formic acid and MeOH. The flow rate was 3.5 mL/min, and gradient elution was carried out as follows: 0–1 min, 5% MeOH; 1–6 min, 5→100% MeOH; 6–10 min, 100% MeOH, resulting in the isolation of CON1 (Rf = 8.31 min). The solvent was removed under reduced pressure, and the residue was dissolved in DCM. The organic layer was washed several times with aqueous $NaHCO_3$ solution, saturated aqueous NaCl solution, and dried over anhydrous Na_2SO_4. After filtration, the solvent was removed by rotary evaporation under reduced pressure. Compound CON1 was obtained as a dark red powder (29.7 mg, 75%) that softens at 178–180 °C. ^{1}H NMR (400 MHz, $CDCl_3$ + CD_3OD): δ = 7.90 (d, *J* = 6.7 Hz, 1 H, H-C_4Ar(dox)), 7.70 (t, *J* = 8.1 Hz, 1 H, H-C_3Ar (dox)), 7.32 (d, *J* = 8.4 Hz, 1 H, H-C_2Ar(dox)), 7.25–7.10 (m, 4 H, 4 x H-Ar(scl)), 6.40 (d, *J* = 16.4 Hz, 1 H, =CH), 6.19 (d, *J* = 16.3 Hz, 1 H, =CH), 5.40 – 5.35 (brs, 1 H, H-2'), 5.17 – 5.10 (m, 1 H, H-C_{10}Ar(dox)), 4.61 (s, 2 H, CH_2-OH), 4.02 (d, 1 H, *J* = 6.7 Hz, H-6'), 4.00 – 3.90 (m, 1 H, H-4'), 3.97 (s, 3 H, -O-CH_3), 3.86 (s, 2 H, Ar-CH_2-NH), 3.50 – 3.45 (brs, 1 H, H-5'), 3.20 – 3.00 (m, 3 H, CH_2NHCO-, H-C_7Ar(dox)), 3.00 – 2.85 (m, 1 H, H-C_7Ar(dox)), 2.80 – 2.70 (m, 2 H, -CH_2NHCH_2Ar-), 2.40 – 2.10 (m, 5 H, -$NHCOCH_2CH_2CONH$ and H-C_9Ar(dox)), 2.05 – 1.90 (m, 1 H, H-C_9Ar(dox)), 1.85 – 1.65 (m, 4 H, H-$C_{3'}$Ar(dox)), 1.65 – 1.35 (m, 6 H, H-$C_{3'}$Ar(dox)), 1.30 – 1.20 (m, 3 H), 1.23 (s, 3 H, Me), 1.05 – 0.90 (m, 2 H), 1.16 (d, *J* = 6.7 Hz, 3 H, $C_{6'}$-CH_3), 1.04 (s, 3 H, Me), 0.90 – 0.75 (m, 2 H), 0.74 (s, 3 H, Me), 0.68 (s, 3 H, Me), 0.67 (s, 3 H, Me) ppm. ^{13}C NMR (101 MHz, $CDCl_3$ + CD_3OD): δ = 213.65 (C13=O), 187.14 (C12=O), 186.71 (C5=O), 174.33 (NHC=O), 172.20 (NHC=O), 161.00 (C1), 155.92 (C6), 155.19 (C11), 139.42 (=CH), 138.48, 135.88 (C3), 135.36 (C4a), 133.86 (C10a), 133.60 (C6a), 129.82 (2 x Ar(scl)), 126.83 (2 x Ar(scl)), 126.53, 125.26 (=CH), 120.71(C12a), 119.75 (C4), 118.61 (C2), 111.46 (C5a), 111.25 (C11a), 100.69 (C2'), 77.36, 76.33 (C8), 74.49, 73.06, 69.37 (C10), 68.28 (C5'), 67.41 (C6'), 65.05 (C14), 61.38, 56.54 (O-CH_3), 56.05, 51.31 (Ar-CH_2-NH), 45.55, 45.00, 44.50 (NH-C4'), 43.68, 41.90, 39.66, 39.18, 36.03, 35.69 (C9), 33.54 (C7), 33.21 (Me), 33.11, 31.03, 29.60, 29.28 (C3'), 26.20, 23.64 (Me), 21.32 (Me), 20.32 (Me), 18.91, 18.34, 16.64 (6'-CH_3), 15.30 (Me) ppm. HRMS (HESI/Orbitrap) m/z: $[M + H]^+$ Calcd for $C_{61}H_{82}O_{15}N_3$ 1096.57405; Found 1096.57532. IR (ATR): ν = 3360, 2926, 1724, 1618, 1577, 1444, 1411, 1387, 1284, 1236, 1209, 1170, 1116, 1083, 1018, 985, 794, 765, 611, 463 cm^{-1}. HPLC purity, method A: t_R = 8.309 min, area 96.13%. Method B: t_R = 6.688 min, area 95.32% (λ = 254 nm). $[\alpha]_D^{25}$ + 0.012 (c = 1.7 $\times 10^{-4}$ g/mol, MeOH).

2.1.5. Synthesis of CON2: N1-((2 S,3 S,4 S,6 R)-3-hydroxy-2-methyl-6-(((1 S,3 S)-3,5,12-trihydroxy-3-(2-hydroxyacetyl)-10-methoxy-6,11-dioxo-1,2,3,4,6,11-hexahydrotetracen-1-yl)oxy)tetrahydro-2 H-pyran-4-yl)-N4-(6-((4-((R,E)-3-hydroxy-5-((1 R,2 R,4aS,8aS)-2-hydroxy-2,5,5,8a-tetramethyldecahydronaphthalen-1-yl)-3-methylpent-1-en-1-yl)benzyl)amino)hexyl)succinamide

In a solution of doxorubicin hydrochloride (15 mg, 0.052 mmol) in dry DMF (500 µL), diisopropylethylamine (13 µL, 0.036 mmol) was added. The addition of DIEA caused the solution to change color from light red to dark red. The reaction mixture was left stirring at room temperature for 30 minutes under argon, followed by the addition of compound LIG2 (16 mg, 0.026 mmol). After cooling the reaction mixture in an ice bath (0 °C), solutions of HOBT (8.9 mg, 0.036 mmol) and EDCI (14 mg, 0.036 mmol) in dry DMF (100 µL each) were added sequentially. The reaction mixture was stirred for 30 minutes at 0 °C and then for 18 h at room temperature in the dark. The reaction progress was monitored using an Agilent 1200 HPLC system equipped with a reverse-phase analytical InfinityLab Poroshell 120 CS-C18 column (4.6 × 100 mm, 2.7µ, S.N. USKBM01053). The mobile phase consisted of a mixture of 0.1% aqueous formic acid and ACN with a programmed isocratic and gradient elution: 0–1 min, 5% ACN; 1–6 min, 5%→95% ACN; 6–12 min, 95% ACN; 12–14 min, 95% A→5% ACN; 14–15 min, 5% ACN. The flow rate was 0.6 mL/min. Signal detection was performed in the wavelength range of 254/280 nm using a DAD detector. After 12 h, the reaction was stopped, and the reaction mixture was concentrated under reduced pressure. The crude reaction mixture was purified on an HPLC-DAD system using a semi-preparative ZORBAX Eclipse XDB-C18 column (9.4 × 250 mm, 5µ, S.N. USSY004729) (DAD detector: 254 nm). The mobile phase consisted of a mixture of 0.1% aqueous formic acid and MeOH. The flow rate was 3.5 mL/min, and gradient elution was carried out as follows: 0–1 min, 5% MeOH; 1–6 min, 5→100% MeOH; 6–10 min, 100% MeOH, resulting in the isolation of CON2 (Rf = 8.33 min). The solvent was removed under reduced pressure, and the residue was dissolved in DCM. The organic layer was washed several times with aqueous $NaHCO_3$ solution, saturated aqueous NaCl solution, and dried over anhydrous Na_2SO_4. After filtration, the solvent was removed by rotary evaporation under reduced pressure. Compound CON2 was obtained as a dark red powder (21.3 mg, 75%) that softens at 170–172 °C. ^{1}H NMR (400 MHz, $CDCl_3$ + CD_3OD): δ = 7.86 (d, J = 8.7 Hz, 1 H, H-C_4Ar(dox)), 7.65 (t, J = 8.1 Hz, 1 H, H-C_3Ar (dox)), 7.28 (d, J = 8.7 Hz, 1 H, H-C_2Ar(dox)), 7.21 (d, J = 8.2 Hz, 2 H, 2 x H-Ar(scl)), 7.14 (d, J = 7.9 Hz, 2 H, 2 x H-Ar(scl)), 6.38 (d, J = 16.4 Hz, 1 H, =CH), 6.14 (d, J = 16.1 Hz, 1 H, =CH), 5.35 – 5.30 (brs, 1 H, H-2'), 5.13 – 5.07 (m, 1 H, H-C_{10}Ar(dox)), 4.59 (s, 2 H, CH_2-OH), 3.99 – 3.95 (m, 1 H, H-6'), 3.95 – 3.85 (m, 1 H, H-4'), 3.91 (s, 3 H, -O-CH_3), 3.74 (s, 2 H, Ar-CH_2-NH), 3.40 – 3.35 (brs, 1 H, H-5'), 3.12 – 3.02 (m, 1 H, H-C_7Ar(dox)), 2.96 (t, J = 6.6 Hz, 2 H, -CH_2NHCO-), 2.92 – 2.82 (m, 1 H, H-C_7Ar(dox)), 2.57 (t, J = 7.3 Hz, 2 H, -CH_2NHCH_2Ar-), 2.40 – 2.10 (m, 5 H, -$NHCOCH_2CH_2$CONH and H-C_9Ar(dox)), 2.10 – 1.90 (m, 1 H, H-C_9Ar(dox)), 1.85 – 1.75 (m, 1 H, H-$C_{3'}$Ar(dox)), 1.70 – 1.50 (m, 4 H, H-$C_{3'}$Ar(dox)), 1.50 – 1.35 (m, 6 H), 1.35 – 1.15 (m, 6 H), 1.18 (s, 3 H, Me), 1.15 – 1.05 (m, 5 H), 1.05 – 0.95 (m, 2 H), 1.12 (d, J = 6.6 Hz, 3 H, 6'-CH_3), 0.85 – 0.70 (m, 2 H), 0.98 (s, 3 H, Me), 0.85 – 0.70 (m, 2 H), 0.69 (s, 3 H, Me), 0.63 (s, 3 H, Me), 0.61 (s, 3 H, Me) ppm. ^{13}C NMR (101 MHz, $CDCl_3$ + CD_3OD): δ = 213.56 (C13=O), 187.14 (C12=O), 186.67 (C5=O), 172.89 (NHC=O), 172.30 (NHC=O), 160.94 (C1), 155.88 (C11), 155.17 (C6), 138.95 (=CH), 135.83 (C3), 135.30 (C4a), 133.92 (C10a), 133.62 (C6a), 129.39 (2 x Ar(scl)), 126.67 (2 x Ar(scl)), 125.33 (=CH), 120.63 (C12a), 119.65 (C4), 118.58 (C2). 111.41 (C11a), 111.17 (C5a), 100.64 (C2'), 77.36, 76.24 (C8), 74.32, 72.96, 69.33 (C10), 68.22 (C5'), 67.29 (C6'), 64.94 (C14), 61.21, 56.40 (O-CH3), 55.98, 51.48 (Ar-CH_2-NH), 45.47 (NH-C4'), 44.98, 43.55, 41.81, 39.58, 39.10, 38.93, 35.70 (C9), 33.39 (C7), 33.07 (Me), 33.00, 31.18, 31.02, 29.48, 29.16 (C3'), 28.52, 26.07 (Me), 25.94, 23.46 (Me), 21.18 (Me), 20.21, 18.92, 18.23, 16.50 (C6'-CH_3), 15.18 (Me) ppm. HRMS (HESI/Orbitrap) m/z: $[M + H]^+$ Calcd for C64H88O15N3 1138.62100; Found 1138.62158. IR (ATR): ν = 3314, 2932, 2865, 1721, 1582, 1444, 1412, 1385, 1347, 1285, 1209, 1115, 1084, 1017, 986, 792, 764, 587, 478 cm^{-1}. HPLC purity, method A: t_R = 8.336 min, area 98.18%. Method B: t_R = 6.735 min, area 98.75% (λ = 254 nm). $[\alpha]_D^{25}$ + 0.019 (c = 1.7 $\times 10^{-4}$ g/mol, MeOH).

2.2. Compounds

The study investigated the following compounds: sclareol (SC), doxorubicin (DOX), and temozolomide (TMZ). These compounds were purchased from Sigma-Aldrich, Germany. In addition, hybrid compounds of SC and DOX (known as conjugates) CON1 and CON2, along with their corresponding ligands (LIG1 and LIG2), were synthesized using the aforementioned procedure. Initially, all the compounds were dissolved as 20 mM stocks in dimethyl sulfoxide (DMSO) and kept as aliquots at −20 °C. Prior to administration, the compounds were dissolved in sterile deionized water.

2.3. Chemicals and reagents

The following chemicals and reagents were used in the experimental work: Hoechst 33342, DMSO, 3-[4,5-dimethylthiazol-2-yl]-2,5-diphenyltetrazolium bromide (MTT), JC-1, Ham's F12 growth media, hydrocortisone, insulin and adenine (Sigma-Aldrich, Germany), minimal essential medium (MEM), RPMI 1640 medium, Dulbecco's modified minimal essential medium (DMEM), fetal bovine serum (FBS), a mixture of antibiotics penicillin-streptomycin (Capricorn Scientific, Germany), trypsin/EDTA (Biological Industries, USA), L-glutamine, a mixture of antibiotics and antimycotics: penicillin, streptomycin, amphotericin B (Gibco, Thermo Fisher Scientific, USA), MEM non-essential amino acids (Biowest, USA), Annexin-V-FITC (AV) and propidium iodide (PI) Apoptosis Detection Kit (Abcam, UK), Tumor Dissociation Kit (Miltenyi Biotec, Germany), Epidermal growth factor (BioLegend, USA), ribonuclease A (Invitrogen, Thermo Fisher Scientific, USA), dihydroethidium (DHE), dihydrorhodamine 123 (DHR), fluorescein-di-D-galactopyranoside (FDG), Alexa Fluor 488 goat anti-rabbit secondary antibody (#A-11008) (Thermo Fisher Scientific, USA), Anti-phospho-histone H2A.X (Ser139) rabbit (Cell Signaling Technology®, USA), Seahorse XF DMEM assay medium and Seahorse XF Cell Mito Stress Test Kit (Agilent, USA).

2.4. Cells and cell culture

Glioblastoma cell line U87, colorectal carcinoma cell line DLD1 and human non-small cell lung carcinoma cells (NSCLC) NCI-H460 were purchased from the American Type Culture Collection, (ATCC, USA). Multidrug-resistant U87-TxR and DLD1-TxR cells were selected from U87 and DLD1 cells, respectively, by continuous exposure to the stepwise increasing concentrations of paclitaxel (PTX) during six to nine months [35]. Multidrug-resistant NCI-H460/R cells were selected from NCI-H460 cells by continuous exposure to the stepwise increasing concentrations of doxorubicin during three months [36]. Human lung fibroblasts MRC-5 and human glioblastoma cell line U251 were purchased from the European Collection of Authenticated Cell Cultures (ECACC, UK). U87, U87-TxR and MRC-5 were cultivated in MEM supplemented with 10% FBS, 1% L-glutamine, 1% antibiotic mixture of penicillin and streptomycin, and 1% non-essential amino acids. U251 cell line was cultivated in DMEM with 10% FBS, 1% L-glutamine and 1% antibiotic-antimycotic mixture. NCI-H460, NCI-H460/R, DLD1 and DLD1-TxR were grown in RPMI 1640 medium supplemented with 10% FBS, 1% L-glutamine, and 1% antibiotic-antimycotic mixture. All cell lines were grown at 37 °C, in a humid atmosphere with 5% CO_2.

The cells were grown in 25 cm^2 and 75 cm^2 flasks (Thermo Fisher Scientific, USA) until they reached 80–90% confluence. Then, cell passage was carried out using 0.25% trypsin/EDTA. The cells were counted using a Burker-Turk hemocytometer on an inverted microscope after trypsinization. Once counted, the cells were sown at an appropriate density for further experimentation or maintenance in culture. For NCI-H460, NCI-H460/R, DLD1, and DLD1-TxR, the density was 8,000 cells/cm^2, and for U87, U87-TxR, U251, and MRC-5, the density was 16,000 cells/cm^2.

2.5. Primary cell culture

Sample from patient with WHO grade 3 anaplastic astrocytoma (ASC) was collected in April 2023 from the Clinic for Neurosurgery at the Clinical Center of Serbia. The histological grade was established by correlating histopathological analysis of the surgical specimen and neuroradiological examination. The diffuse expression of GFAP, OLIG2, and MAP2 as well as focal expression of vimentin and p53 were confirmed by histopathological analysis. The sample was collected and used in the study after obtaining patients' informed consent and the approval from the Ethics Committee of the Clinical Center of Serbia (ref. number 187/13) and the work was carried out in accordance with The Code of Ethics of the World Medical Association (Declaration of Helsinki) for experiments involving humans. The tissue sample was collected during surgery and immediately processed. Upon arrival, the tissue was manually chopped with a surgical blade in a Petri dish under sterile conditions. The sample was cut into 3 – 5 mm pieces and further dissociated using the Tumor Dissociation Kit. Sample was incubated in a 37 °C orbital shaker (KS 126 4000 ic control, IKA, Königswinter, Germany) at 300 rpm for 90 min. After incubation, the dissociated tissue was placed in DMEM/Ham's F12 (1:3 ratio) growth medium supplemented with 5% FBS, antibiotic-antimycotic solution, 4 μg/mL hydrocortisone, 1 μg/mL insulin, 10 ng/mL epidermal growth factor, 24 μg/mL adenine. Dissociated tissue was cultured in T-25 cell culture flasks until cell attachment was observed before the medium was replaced. Successful patient-derived cultures were maintained at 37 °C in humidified atmosphere with 5% CO_2 and grown to confluence before further experiments.

2.6. Cell growth inhibition

The MTT assay was used to assess how the compounds affected cell viability. The assay works by measuring the activity of the mitochondrial enzyme succinate dehydrogenase, which is a good indicator of mitochondrial respiration and overall metabolic activity of the cell. This indirectly measures the viability of living cells. The experiment lasted for 72 h and at the end of the treatment period, 100 μL of MTT solution (0.2 mg/mL) was added to each well and the plates were incubated at 37 °C with 5% CO_2 for 4 h. The formazan product was dissolved in 100 μL DMSO, and the absorbance of the resulting dye was measured at 570 nm with a reference wavelength of 690 nm using an automatic microplate reader (Multiskan Sky, Thermo Scientific, USA). The IC_{50} value was determined as the concentration of a drug that inhibited cell growth by 50%. The IC_{50} was calculated using non-linear regression analysis with log (inhibitor) vs. normalized response in GraphPad Prism 8.0.2 software.

2.6.1. The effects of SC on the cell growth inhibition

The effects of SC were investigated in eight different cell lines. The cells were seeded in 96-well microtiter plates (SARSTEDT AG & Co. KG, Germany) at a density of 2,000 cells per well for NCI-H460, NCI-H460/R, DLD1, and DLD1-TxR, and 4,000 cells per well for MRC-5, U87, U87-TxR, and U251 in 100 μL of the appropriate medium. Control cells that received no treatment were also seeded at the same time. Increasing concentrations of SC were used (5, 10, 20, 50, and 100 μM).

2.6.2. The evaluation of the resistance and selectivity of SC, DOX, CON1, and CON2

To compare the resistance and selectivity profiles among SC, DOX, CON1, and CON2, human glioblastoma cell lines U87, U87-TxR, and normal fibroblast MRC-5 cells were seeded at a density of 4,000 cells per well in 100 μL of the appropriate medium. The effects of LIG1 and LIG2 were also examined. The range of concentrations differed among the cell lines and the compounds. For LIG1 and LIG2, the used concentrations for all cell lines were 50, 100, 200, 300, and 400 μM, while the same concentrations were used for MRC-5 in the case of SC, CON1, and CON2. DOX concentrations were 0.1, 0.25, 0.5, 1, and 2.5 μM for U87 and 0.25, 0.5, 1, 2.5, and 5 μM for U87-TxR and MRC-5. U87 and U87-TxR cells were treated with 5, 10, 20, 50, and 100 μM of SC and 1, 2.5, 5, 10, and 25 μM of CON1 and CON2.

2.6.3. The effects of DOX, CON1, CON2, and TMZ on ASC cells

To study the effects of DOX, CON1, CON2, and TMZ on ASC primary cells, 4,000 or 8,000 cells/well were seeded in 100 μL of the appropriate medium. The cells were then treated with increasing concentrations of DOX (200, 500, 1000, 2000, and 5000 nM), CON1 and CON2 (2, 5, 10, 20, and 50 μM), and TMZ (20, 50, 100, 200, and 500 μM).

2.7. Chou-Talalay method for drug combination

The CalcuSyn software utilized the Chou-Talalay combination index method to determine the synergistic, antagonistic, or additive interaction of two compounds. This method considers the concentration of each compound, the individual effect of each compound, and their combined effect. The combination index (CI) values indicate the nature of the interaction. A CI value of less than 0.9 indicates that the compounds have a synergistic effect, a value of more than 1.1 indicates an antagonistic effect, and a value between 0.9 and 1.1 indicates an additive effect.

To assess the combined cytotoxic effects of SC and DOX in different cell lines, increasing concentrations of DOX (20, 50, 100, 200, and 500 nM) along with SC (10 and 20 μM) were used. The cells were seeded in 96-well microtiter plates at the density of 2,000 cells per well for NCI-H460, NCI-H460/R, DLD1 and DLD1-TxR, and 4,000 cells per well for MRC-5, U87, U87-TxR, and U251 in 100 μL of the appropriate medium. The experiment was carried out for 72 h.

To investigate the effects of different ratios of SC and DOX at lower concentrations, SC (100, 200, 400, 500 and 1000 nM) was simultaneously combined with DOX (100 and 200 nM) in U87 and U87-TxR cells. This allowed for the ratios of 1:1, 2:1 and 5:1 to be achieved. U87 and U87-TxR cells were seeded at a density of 4,000 cells per well in 100 μL of the appropriate medium.

After 72 h of treatment, we added 100 μL of MTT solution (0.2 mg/mL) to each well and incubated the plates at 37 °C with 5% CO_2 for 4 h. Formazan product was then dissolved in 100 μL DMSO, and the absorbance of obtained dye was measured at 570 nm with a reference wavelength at 690 nm using an automatic microplate reader (Multiskan Sky, Thermo Scientific, USA).

2.8. Real-time ASC cell growth monitoring

The xCELLigence system with a 96-well E-plate was used to monitor the growth of ASC primary culture cells in real time. A standard background was measured by adding 100 μL of media to each well before adding the cells to the E-plate. The cells were then seeded and the total volume of wells was adjusted to 200 μL with media. The cells were treated with increasing concentrations of DOX (200, 500, 1000, 2000, and 5000 nM), CON1 and CON2 (2, 5, 10, 20, and 50 μM), and TMZ (20, 50, 100, 200, and 500 μM). The impedance value of each well was automatically monitored by the xCELLigence system every 30 min for a duration of 186 h and expressed as a CI (cell index) value.

2.9. DOX accumulation assay

DOX fluorescence was utilized to analyze the accumulation of DOX by flow cytometry. DOX, being a P-gp substrate, emits fluorescence whose intensity is proportional to the amount of DOX accumulated. To perform the analysis, cells were counted and suspended in a growth medium. DLD1, DLD1-TxR, NCI-H460, NCI-H460/R, U87, U87-TxR, and U251 cells (100,000 cells per sample) were taken and treated with SC (50 μM) and DOX (20 μM) simultaneously. The samples were then incubated at 37 °C in 5% CO_2 for 60 min. After the accumulation period, the samples were centrifuged, washed twice in cold PBS, and finally resuspended in 1 mL of PBS. The red channel fluorescence of the samples was read on a flow cytometer (Partec, Munster, Germany), and the results were analyzed with Summit 4.3 software (DAKO, CA, USA). At least 10,000 events in each sample were recorded.

2.10. Intracellular distribution of CON1 and CON2

The distribution of DOX-derived fluorescence was analyzed in the U87 glioblastoma cell line after treatment with CON1 and CON2. The cells were initially seeded in a 24-well plate (Thermo Fisher Scientific, USA) at a density of 24,000 cells per well in 600 μL of the appropriate culture medium. After 24 h, the cells were treated with increasing concentrations of CON1 and CON2 (2, 5, and 10 μM), with the treatment lasting for 72 h. The cells were then stained with Hoechst 33342 for 15 min. Following this, all wells were fixed with 4% PFA for 15 min, washed with PBS, and imaged using the ZOE Fluorescent Cell Imager (BIO-RAD, USA) in both the blue and red channels.

2.11. Physicochemical characterization of CON1 and CON2

The physicochemical stability characteristics of the conjugates were analyzed using the Malvern Zetasizer Nano ZS from Malvern Instruments, United Kingdom. The measurement range of the instrument was from 0.6 nm up to 6 mm. The mean size of conjugates, the polydispersity index (PDI), and zeta potential were measured at a temperature of 25 °C. Each sample was diluted 100 times with ultrapure water before measurement. The measurements were repeated three times, and the mean value was presented as the result. PDI is a parameter that defines the size range of particles. The term "polydispersity" (or "dispersity" as recommended by IUPAC) describes the degree of non-uniformity of a size distribution of particles. Zeta potential represents the surface charge of nanoparticles and indicates their long-term stability.

2.12. Chemical modeling

Pharmacokinetic and druglikeness properties were generated using SwissADME web site [37].

Prediction of p*K*a was performed using Epik v5.7 from Schrödinger Suite 2021–3 [38]. Conformational search was performed using Conformational Search from MacroModel v13.3 module from Schrödinger Suite 2021–3 [39], with OPLS4 force field, water as a solvent and mixed torsional/low-mode sampling method. Number of steps was 1000 and energy window for saving the structure (cutoff) was 21 kJ/mol.

2.13. Transmission electron microscopy for CON1 and CON2 characterization and intracellular localization

2.13.1. Detection of nanoparticles

An analysis of the nanoparticles nature of CON1 and CON2 was conducted using transmission electron microscopy (TEM). To prepare for analysis, CON1 or CON2 were diluted 100 times with ultrapure water and Formvar or carbon-coated glow-discharged nickel grids were placed on top of the drops and left for 2–5 min to absorb excess fluid. The particles were examined on a Philips CM12 transmission electron microscope (Philips/FEI, Netherlands) operating at 80 kEV and equipped with the digital camera SIS MegaView III (Olympus Soft Imaging Solutions, Germany). The diameter of CON1 and CON2 particles was measured using iTEM software.

2.13.2. Intracellular localization

For the transmission electron analysis of CON1 and CON2 U87 cell import, 2,000,000 U87 cells were treated 24 h with 5 μM CON1 or CON2, while untreated cells served as controls. Immediately after treatment, cells were rinsed with PBS, fixed with 2.5% glutaraldehyde in 0.1 M cacodylate buffer (pH 7.2) for 2 h at 4 °C, and rinsed again in cacodylate buffer. The cells were then postfixed in 2% osmium tetroxide in the same buffer, dehydrated using increasing concentrations of ethanol, and embedded in resin. Semi-fine sections were used for electron microscopy trimming, and ultra-thin sections of cells were obtained using a Leica UC6 ultramicrotome (Leica Microsystems, Germany) and mounted on copper grids. Over 20 cell sections were examined on a Philips CM12 transmission electron microscope equipped with the digital camera SIS MegaView III. The resulting electron micrographs were used for overall U87 cell morphological analysis and CON1 or CON2 cell import analysis.

2.14. Double strand DNA breaks detection

To quantify the DNA damage in U87 and U87-TxR cells, the fluorescence intensity of anti-phospho-histone H2A.X antibody was used. The antibody detects endogenous levels of phosphorylated H2A.X, which is recruited to double strand DNA breaks sites. The cells were seeded at a density of 100,000 cells/well in 6-well tissue culture plates and grown overnight. After that, the cells were treated with 2, 5, 10 and 20 μM DOX, CON1 and CON2 for 24 h at 37 °C. The cells were then harvested, washed in PBS, and fixed in 4% PFA for 15 min at room temperature. Next, the cells were permeabilized with ice-cold 90% methanol for 90 minutes at −20 °C. After washing in PBS, the cells were blocked with 0.5% BSA in PBS for 1 h, and then incubated overnight at 4 °C with anti-phospho-histone H2A.X antibody diluted 1:500 in 0.5% BSA in PBS. Following washing in PBS, the cells were incubated for 30 min at room temperature with fluorescent Alexa Fluor 488 anti-rabbit IgG (H + L) secondary antibody diluted 1:1000 in 0.5% BSA in PBS. The cells were then washed and resuspended in 1 mL of PBS. The green fluorescence intensity was measured at 525 nm on the CytoFLEX flow cytometer (Beckman Coulter, IN, USA). At least 10,000 events in each sample were recorded, and the results were analyzed in CytExpert software (Beckman Coulter, IN, USA).

2.15. Reactive oxygen and nitrogen species, and changes in mitochondrial membrane potential detection

The levels of reactive oxygen species (ROS) and reactive nitrogen species (RNS), as well as changes in mitochondrial membrane potential, were measured in U87 glioblastoma cells using flow cytometry on the CytoFLEX flow cytometer from Beckman Coulter. The production of superoxide anion was detected using DHE, which only emits fluorescence in the presence of superoxide anion. The fluorescence of DHR was used to detect hydrogen peroxide and peroxynitrite anions. This dye only emits fluorescence when these anions are present. Changes in mitochondrial membrane potential were studied using JC-1, a ratiometric dye that detects the transition from red fluorescent aggregates to green fluorescent monomers. An increase in green fluorescence indicates a decrease in mitochondrial membrane potential.

To perform the experiments, U87 glioblastoma cells were seeded in 6-well plates at a density of 100,000 cells per well and incubated overnight. The cells were then treated with 2 μM DOX, CON1, and CON2 for 24 h. The adherent cells were stained with DHE, DHR, or JC-1 for 30 min at 37 °C in the dark. After staining, the cells were harvested by trypsinization and washed twice with PBS. The CytoFLEX flow cytometer from Beckman Coulter was used to analyze DHE red fluorescence (at 585 nm), DHR green fluorescence (at 525 nm), and JC-1 green/red fluorescence (525/585 nm). At least 10,000 events were assayed for each sample.

2.16. Mitochondrial respiration measurement on SeaHorse XF HS Mini Analyzer

The rate of OXPHOS was measured using a Seahorse XF HS Mini

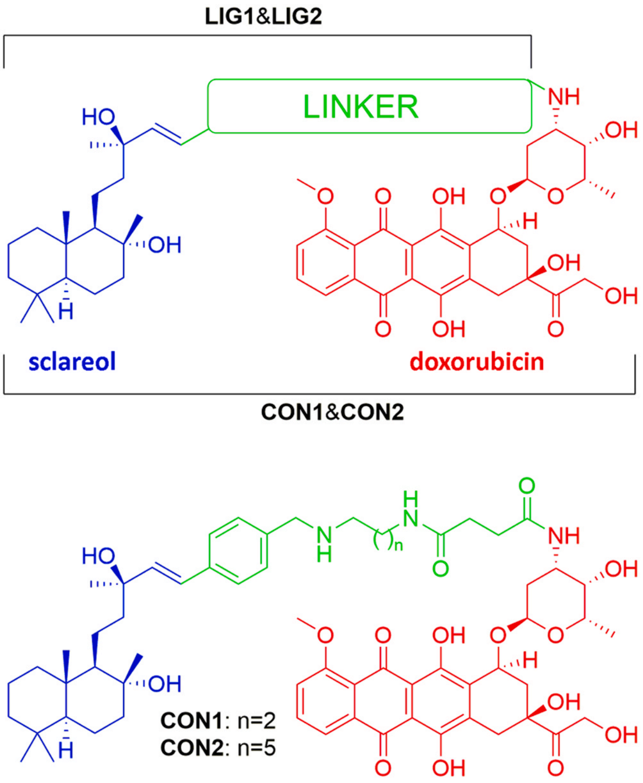

Fig. 1. The structures of hybrid compounds of SC and DOX - conjugates CON1 and CON2. In the upper panel the general structure of SC and DOX hybrid compounds is provided. The upper panel shows the general structure of these hybrid compounds, while the lower panel shows the structure of CON1 and CON2 along with their corresponding ligands, LIG1 and LIG2. The difference between ligands/conjugates is the length of the linker, which is either n=2 (LIG1/CON1) or n=5 (LIG2/CON2), where n represents the number of carbon atoms in the linker.

Table 1
Anticancer effects of DOX, SC, CON1, CON2, LIG1, and LIG2 expressed in IC_{50} values.

	U87	U87-TxR[b]	Relative Resistance[c]	MRC-5	Selectivity Index[d]
DOX[a]	100.1	1323.9	13.2	294.6	2.9
SC	51.6	39.2	0.8	75.9	1.5
CON1	8.8	28.7	3.3	137.2	15.6
CON2	6.2	26.2	4.2	>400	>64.5
LIG1	74.4	61.7	0.8	236.0	3.2
LIG2	344.6	273.1	0.8	>400	>1.2

[a] IC_{50} values for DOX are in nanomoles, and for other compounds in micromoles.

[b] Multidrug resistant (MDR) cancer cell line obtained by continuous exposure to paclitaxel

[c] The relative resistance obtained as the ratio between the IC_{50} value for the MDR cancer cell line and the corresponding sensitive cell line.

[d] Selectivity index obtained as a ratio between the IC_{50} value for MRC-5 and the corresponding sensitive cell line.

analyzer (Agilent, USA). For the mitochondrial stress test, 4,000 U87 glioblastoma cells were plated in Seahorse XF HS Mini plates using 80 µL of appropriate medium. The cells were then incubated overnight before being treated with 5 µM DOX and 5 µM CON1 for 24 h at 37 °C in a humidified incubator with 5% CO_2. One hour before the XF assay, the cells were washed and left in an XF DMEM medium in a humidified atmosphere without CO_2. Basal Oxygen Consumption Rate (Oxygen Consumption Rate) measurements were made in XF DMEM without supplementation. Using the Seahorse XF Cell Mito Stress Test Kit, basal respiration, proton leak, spare capacity, maximal respiration, non-mitochondrial respiration, and ATP production were measured through OCR. This was done after the sequential injection of Oligomycin, FCCP, and Rotenone & antimycin A.

2.17. *Cell cycle analysis*

U87 glioblastoma cells were seeded in 6-well plates at a density of 200,000 cells per well and allowed to settle overnight. The effects of 2 µM DOX, 2 µM CON1, and 20 µM CON1 on cell cycle distribution were studied after 48 h. In addition, ASC primary cells were seeded at a density of 100,000 cells per well and treated with 1 µM DOX, 10 µM CON1, and 10 µM CON2 for 48 h. The cells were then trypsinized, collected by centrifugation, washed with PBS, and fixed in 70% ethanol for 24 h at −20 °C. After fixation, the cells were washed with PBS, pretreated with 50 µg/mL of ribonuclease A, and incubated at 37 °C for 15 min. Then, PI was added to the final 2 µg/mL concentration. Flow cytometric analysis was performed on the CytoFLEX flow cytometer (Beckman Coulter, IN, USA). At least 10,000 events were collected for each experimental sample, and cell cycle distribution was determined using CytExpert software (Beckman Coulter, IN, USA).

2.18. *Cell death detection*

The Apoptosis Detection Kit assessed apoptotic, necrotic, and viable cell percentages. Annexin-V-FITC and PI staining were carried out as per the manufacturer's instructions. ASC primary cells were seeded in 6-well tissue culture plates with a density of 100,000 cells per well. The cells were then treated with 1 µM DOX, 10 µM CON1, and 10 µM CON2 for 72 h. After treatment, cells were stained with AV/PI and analyzed by flow cytometry. The CytoFLEX flow cytometer (Beckman Coulter, IN, USA) was used to measure fluorescence intensity in the green (525 nm) and red (585 nm) channels. Each sample recorded at least 10,000 events, and CytExpert software (Beckman Coulter, IN, USA) was used to analyze the percentages of viable (AV- PI-), early apoptotic (AV+ PI-), late apoptotic (AV+ PI+), and necrotic (AV- PI+) cells.

2.19. *β-Galactosidase activity assay*

To measure the activity of β-galactosidase in senescent cells, the FGD substrate's fluorescence was analyzed using flow cytometry. U87 cells were seeded in 6-well plates at a density of 200,000 cells per well and left to incubate overnight. The cells were then treated with either 2 µM DOX, 2 µM CON1, or 20 µM CON1 for 72 h. The adherent cells were trypsinized, and the floating cells were collected. The cells were suspended in an appropriate medium, pre-warmed to 37 °C, and mixed with FDG (200 mM, 1:1, DMSO:H_2O) solved to 2 mM, which was also pre-warmed to 37 °C in sterile H_2O. The cells and FDG solution were rapidly mixed in a 1:1 ratio and incubated for 1 min at 37 °C. Subsequently, 1 mL of ice-cold PBS with 0.2 µg of PI was added to the cells, and they were stored on ice until analysis on the CytoFLEX flow cytometer (Beckman Coulter, IN, USA) in the 525 nm green channel. Dead cells were excluded from the study by excluding those that took up PI. The CytExpert software (Beckman Coulter, IN, USA) was used to analyze the data, and at least 10,000 events were assayed for each sample.

2.20. *Statistical analysis*

The IC_{50} values obtained from the MTT assay were calculated through nonlinear regression analysis using GraphPad Prism 8.0.2 for Windows (San Diego, CA, USA). The results of phospho-histone H2A.X expression, cell death induction, and cell cycle distribution were analyzed by two-way-ANOVA Dunnett's multiple comparisons test using GraphPad Prism 8.0.2 (San Diego, CA, USA). For the FDG accumulation assay, the ordinary one-way ANOVA Dunnett's multiple comparisons test was used to analyze the results.

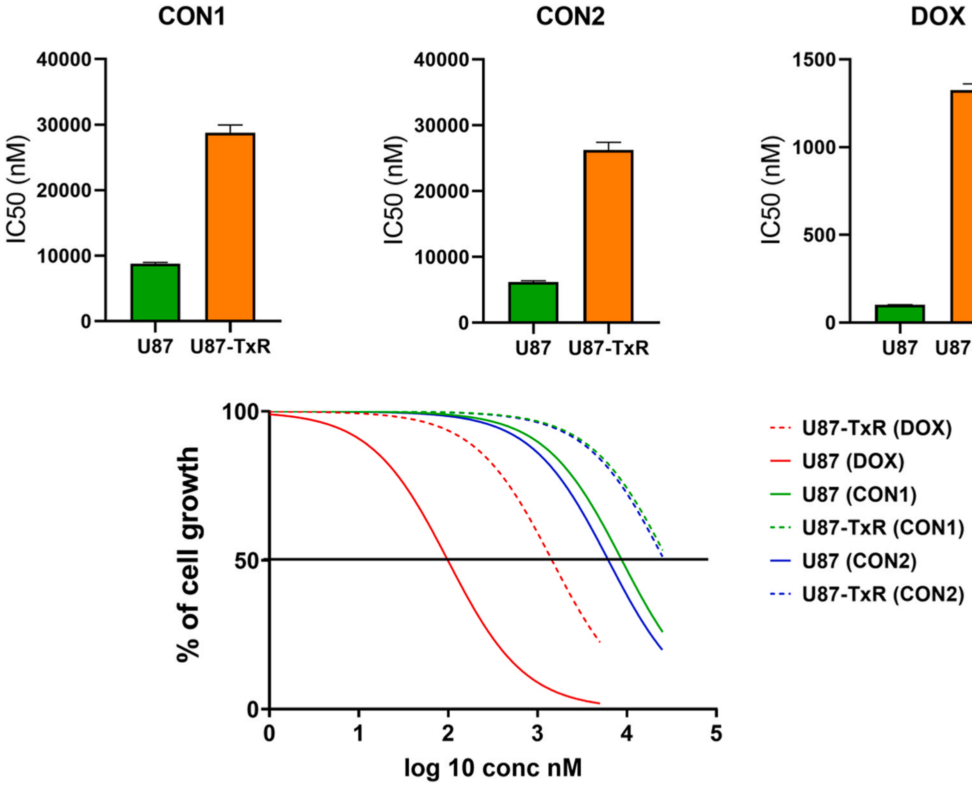

Fig. 2. The resistance profiles of CON1, CON2, and DOX in glioblastoma model comprised of sensitive U87 and resistant U87-TxR cell lines. The concentrations used for CON1 and CON2 ranged from 1.0 μM to 25 μM, while DOX concentrations ranged from 0.25 μM to 5 μM. The treatment lasted for 72 h, and the MTT assay was conducted. Non-linear regression and IC_{50} values were obtained using GraphPad Prism 8.0.2 software. The IC_{50} values for CON1, CON2, and DOX are shown in the upper panel, while the lower panel shows a non-linear function of cell growth inhibition.

3. Results

3.1. The anticancer effects of SC and its combination with DOX

SwissADME analysis revealed that SC has the ability to cross both the human intestine and the blood-brain barrier, and is not a substrate for P-gp (Supplementary Fig. 1). The anticancer effect of SC was found to be relatively weak, with an IC_{50} ranging from 20 μM to 70 μM depending on the cell line (Supplementary Fig. 2). The most significant anticancer effect of SC was observed in colorectal carcinoma cells (DLD1 and DLD1-TxR), with an IC_{50} value of around 20 μM. Notably, collateral sensitivity was observed in glioblastoma cells, where the IC_{50} value in resistant U87-TxR cells was lower than in sensitive U87 cells. In NSCLC cells (NCI-H460 and NCI-H460/R), SC exhibited a moderate anticancer effect, with an IC_{50} of approximately 40 μM. Importantly, in normal human fibroblasts MRC-5, the IC_{50} value was the highest, around 70 μM, indicating selectivity (Supplementary Fig. 2).

The simultaneous combinations between SC and DOX were tested on different cell lines to determine the nature of SC and DOX interaction (Supplementary Fig. 3). The results showed that SC and DOX had a synergistic effect on glioblastoma cells U87-TxR and U251, as well as on resistant NSCLC NCI-H460/R, with $CI < 1$ (Supplementary Fig. 3). On the other hand, SC and DOX exerted an additive effect on sensitive glioblastoma U87 and NSCLC NCI-H460 cells, with $CI \approx 1$. However, SC and DOX showed an antagonistic effect on both colorectal carcinoma cell lines (DLD1 and DLD1-TxR), as well as on normal lung fibroblasts MRC-5, with $CI > 1$ (Supplementary Fig. 3).

Notably, SC increased the accumulation of DOX in glioblastoma cells, regardless of the expression and activity of P-gp. This effect was observed in all examined glioblastoma cell lines, including U87, U87-TxR, and U251 (Supplementary Fig. 4). Especially in resistant cell line U87-TxR, the effect was the most pronounced, with increased accumulation of over 50%, compared to control. In NSCLC cells, DOX accumulation was increased only in resistant NCI-H460/R cells, while in colorectal carcinoma cells (DLD1 and DLD1-TxR), SC failed to raise the DOX accumulation (Supplementary Fig. 4).

Additionally, we tested simultaneous combinations of SC and DOX at lower concentrations in ratios 1:1, 2:1, and 5:1 in glioblastoma cells U87 and U87-TxR. All the examined combinations showed a synergistic effect with $CI < 1$, while this effect was more prominent in U87-TxR, suggesting stronger synergism in resistant U87-TxR than in sensitive U87 glioblastoma cell line (Supplementary Fig. 5).

3.2. The resistance and selectivity profiles of novel hybrid compounds CON1 and CON2

Two hybrid compounds, CON1 and CON2, were synthesized by covalently linking two distinct SC derivative ligands, LIG1 and LIG2, respectively, to DOX via an amide bond (Supplementary Schemes 1–4). The compounds were linked in a 1:1 molar ratio to ensure simultaneous delivery of both chemical entities to cancer cells (Fig. 1). The cytotoxic effects of CON1 and CON2, along with their corresponding SC derivative ligands, LIG1 and LIG2, were tested on glioblastoma and normal human fibroblast cells. The results showed that CON1 and CON2 efficiently inhibited the growth of U87 cells with IC_{50} values below 10 μM (Table 1, Fig. 2). However, the tested SC ligands, LIG1 and LIG2, did not exhibit significant anticancer activity (Table 1). Nonetheless, LIG1 and LIG2 preserved the same collateral sensitivity as SC with the relative resistance (0.8), making them more efficient in resistant U87-TxR cells than in sensitive U87 cells (Table 1). DOX was found to be efficient in the nanomolar range in U87 cells, while in the micromolar range in U87-TxR cells, showing the greatest relative resistance and the lowest selectivity index compared to CON1 and CON2 (Table 1). The hybrid compounds were found to be selective towards cancer cells, as they had

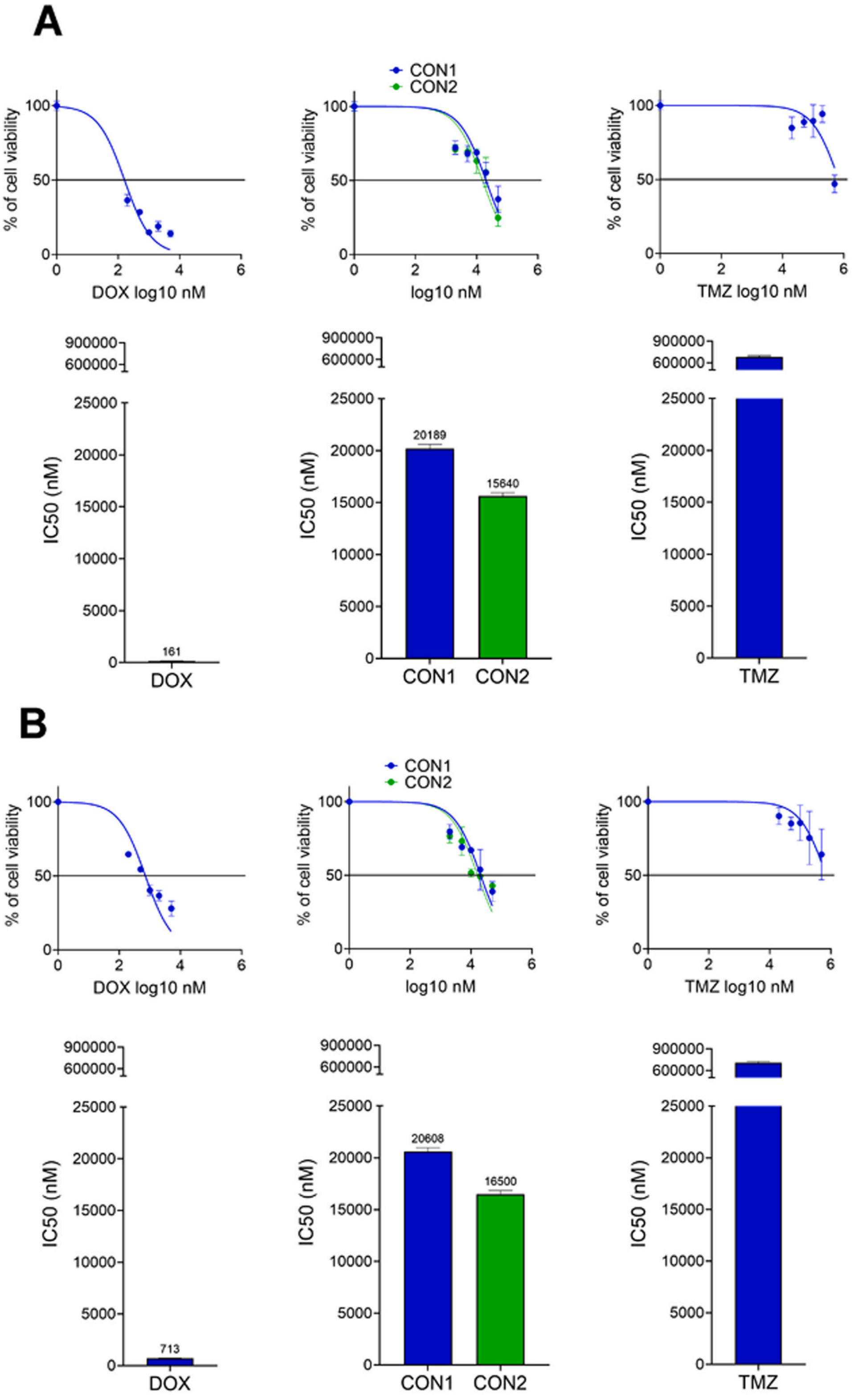

Fig. 3. The effects of DOX, CON1, CON2, and TMZ on the cell growth of ASC patient-derived cells. Primary ASC cells were treated with increasing concentrations of DOX (200, 500, 1000, 2000, and 5000 nM), CON1 and CON2 (2, 5, 10, 20, and 50 μM), and TMZ (20, 50, 100, 200, and 500 μM). In two experimental settings, (**A**) 4000 and (**B**) 8000 primary ASC cells were seeded per well in 96-well plates. The MTT assay was applied after 72 h of treatment. The non-linear function of cell growth inhibition and IC_{50} values were obtained by non-linear regression using GraphPad Prism 8.0.2 software.

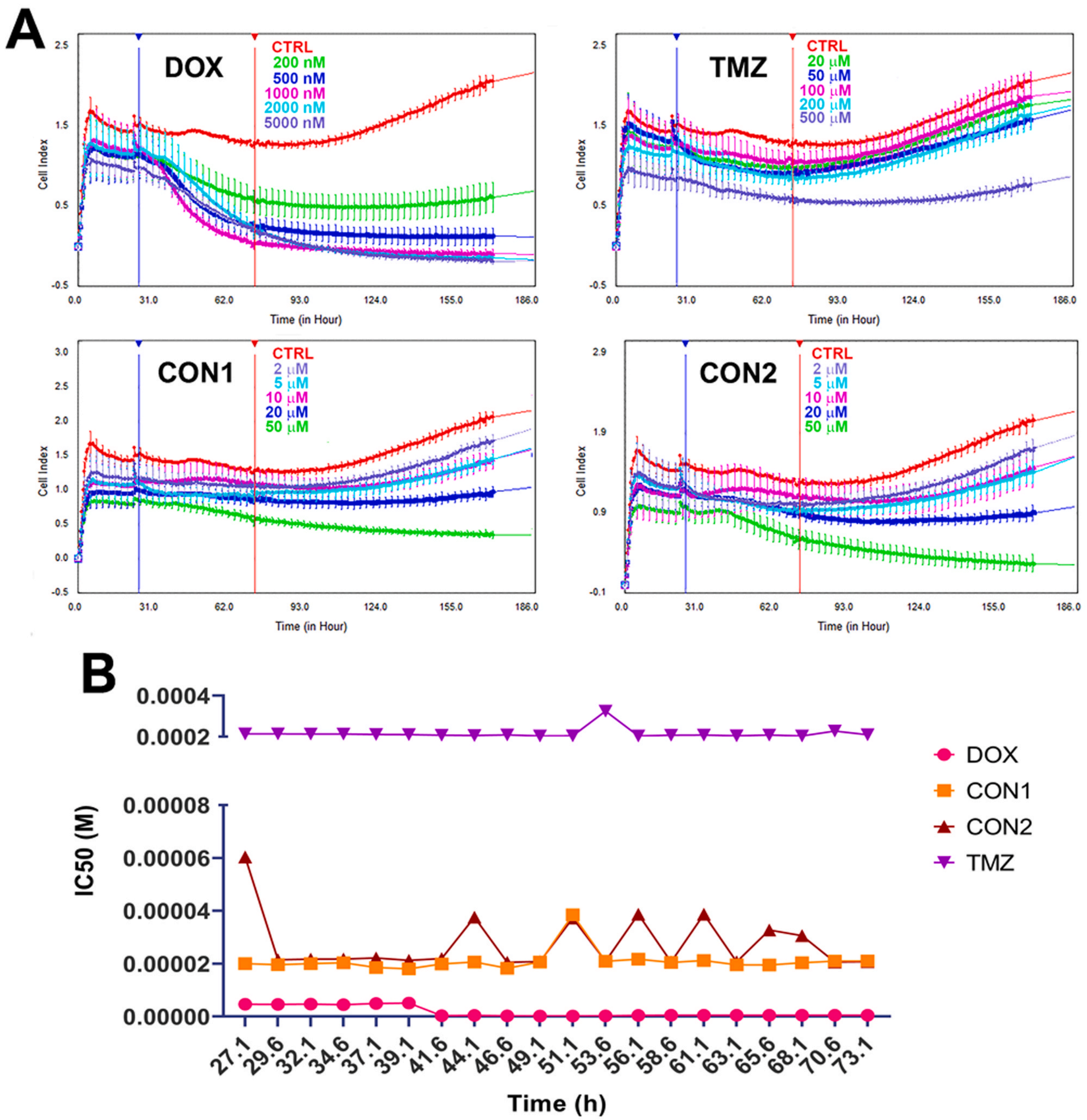

Fig. 4. Real time analysis of DOX, TMZ, CON1, and CON2 effects on ASC patient-derived cell growth. The rate of cell proliferation was monitored for 186 h using the xCELLigence system. The results were obtained by treating primary ASC cells with increasing concentrations of DOX (200, 500, 1000, 2000, and 5000 nM), CON1 and CON2 (2, 5, 10, 20, and 50 μM) and TMZ (20, 50, 100, 200, and 500 μM). (**A**) The Cell Index (CI) of control cells (red line) was compared with the CI of cells treated with increasing concentrations of the drug (other color lines) to determine the impact of the drugs on cell growth. The blue and red vertical lines in the graph (**A**) indicate the time frame of 27–73 h for obtaining the IC_{50} values in (**B**). The results were analyzed using RTCA software for single plate (SP) analyses.

no significant effect on the growth of lung fibroblasts MRC-5 (Table 1). Furthermore, CON1 and CON2 showed lower relative resistance (3.3 and 4.2, respectively) compared to DOX (13.2) in glioblastoma cellular models comprised of sensitive U87 and resistant U87-TxR cells (Table 1, Fig. 2). Additionally, the selectivity index was greater for CON1 and CON2 than for DOX and SC.

3.3. *The anticancer effects of CON1 and CON2 on ASC patient-derived cells*

Next, we assessed the cytotoxic effects of our new hybrid compounds on ASC cells, which were obtained from a patient with anaplastic astrocytoma grade 3 according to pathohistology and neuroradiology examinations. We used temozolomide (TMZ) as a positive control, which is a standard chemotherapeutic for astrocytoma and glioblastoma patients. We compared the anticancer effects of DOX, CON1, CON2, and TMZ at different cell densities of 4000 and 8000 cells per well. According to the results (Fig. 3A and B), TMZ showed the weakest effect, with IC_{50} values above 600 μM. On the other hand, CON1 and CON2 exhibited similar IC_{50} values of 20 μM and 16 μM, respectively, in primary ASC cells, regardless of the cell density. The effect of DOX, however, was dependent on cell density. The IC_{50} values were around 160 nM and 710 nM for 4000 and 8000 cells per well, respectively (Fig. 3A and B).

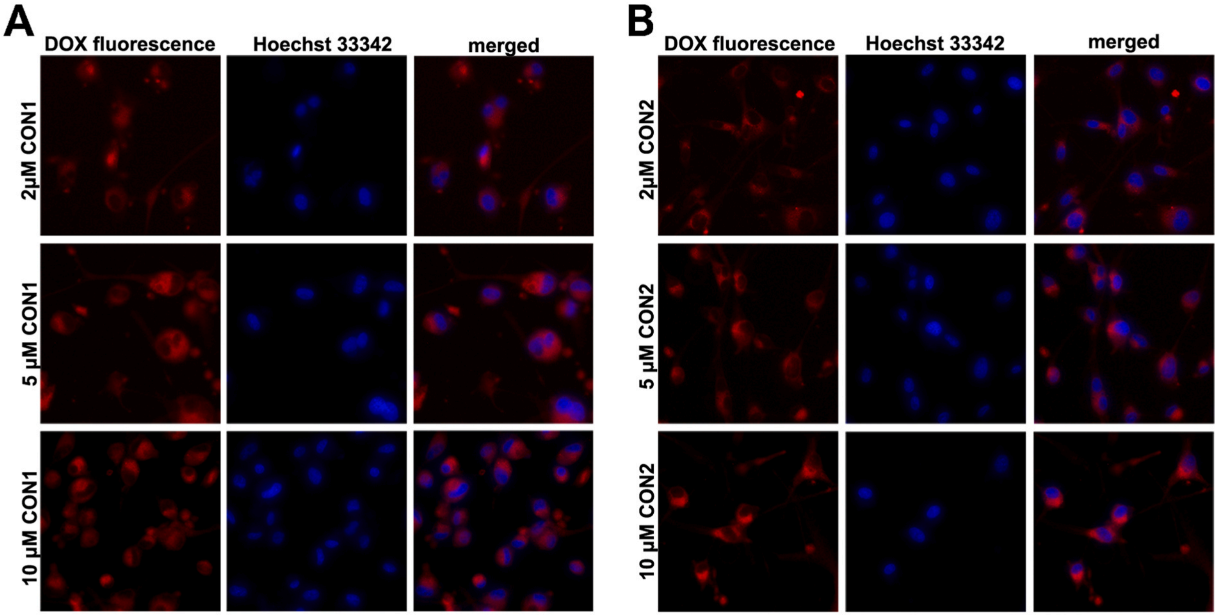

Fig. 5. Intracellular distribution of DOX-derived fluorescence of CON1 and CON2 in U87 glioblastoma cells. The cells were treated with 2, 5, and 10 μM of CON1 (**A**) and CON2 (**B**), and the treatment lasted for 72 h. The perinuclear fluorescence of CON1 and CON2 appears in the red channel, indicating that the fluorescence originates from around the nucleus. The nuclei were contrasted with Hoechst 33342 and appear in the blue channel. The micrographs were obtained using a fluorescent cell imager.

Table 2
Nanoparticle nature of CON1 and CON2 studied by Zetasizer.

	Z-Average (d. nm)	Polydispersity index (PdI) < 0.2	Zeta Potential (mV) > 20
CON1	189.4 ± 9.7	0.198 ± 0.038	39.6 ± 4.3
CON2	180 ± 14.7	0.103 ± 0.016	40.2 ± 1.0

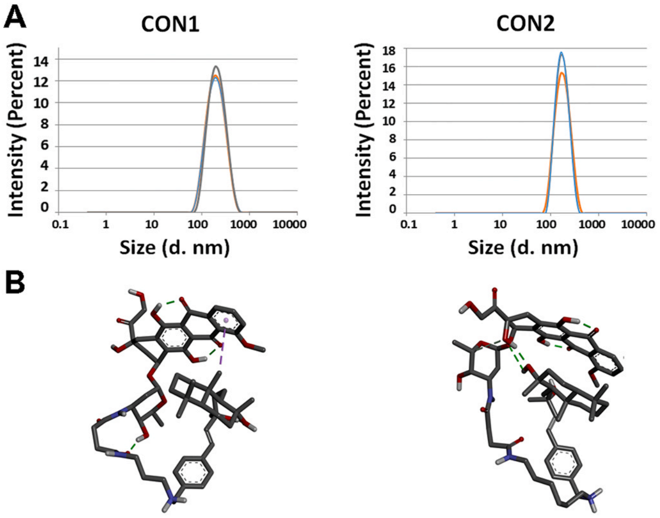

Fig. 6. Physico-chemical characteristics of CON1 and CON2. (**A**) The nanoparticle nature of CON1 and CON2 was discovered using Zetasizer. The size and dispersity of the nanoparticles were measured three times independently. (**B**) The chemical modeling of corresponding CON1 and CON2 predicted that strong intramolecular forces can lead to a spontaneous, "protein-like" folding of CON1 and CON2, forming the nanoparticles.

The efficacy of DOX, CON1, CON2, and TMZ in inhibiting the growth of ASC cells was evaluated using the RTCA xCELLigence system (Fig. 4). The system monitored the impedance-based Cell Index (CI) of the cells for 186 h, which was used to determine their growth rate (Fig. 4A). The antiproliferative effect refers to a decrease in cells' growth rate, but the growth pattern still follows the same path as untreated cells (Fig. 4A). The cytostatic effect corresponds to the cell growth profile on the same baseline as the seeded cells (Fig. 4A). The cytotoxic effect refers to a drop in the cell growth profile below the seeded cells' baseline (Fig. 4A). The IC_{50} values were calculated between 27 h and 73 h (Fig. 4B) to replicate the endpoint MTT assay which lasted 72 h. The cytostatic effect of DOX treatment of ASC cells was observed at 200 nM, whereas higher concentrations ranging from 500 to 5000 nM were cytotoxic (Fig. 4A). The IC_{50} values for DOX were around 5 μM until 40 h and then dropped to around 400 nM (Fig. 4B), which was consistent with the endpoint MTT assay results. In the case of TMZ, concentrations ranging from 20 to 200 μM were antiproliferative, while only the highest concentration of 500 μM showed a cytostatic effect (Fig. 4A). The IC_{50} values of TMZ were around 200 μM (Fig. 4B). CON1 and CON2 showed similar effects in this experimental setting, exhibiting an antiproliferative effect with 2, 5, and 10 μM, cytostatic with 20 μM, and cytotoxic effect with 50 μM (Fig. 4A). The IC_{50} values for both CON1 and CON2 were approximately 20 μM with greater fluctuations observed in the case of CON2 (Fig. 4B).

3.4. Physicochemical characterization and intracellular localization of CON1 and CON2

We used the preserved fluorescence from the DOX part of the hybrid compound to analyze where our novel hybrids CON1 and CON2 were located inside cells (Fig. 5). After treating U87 cells with three different concentrations of 2, 5, and 10 μM for 72 h, we found that both CON1 and CON2 were located near the nuclear membrane (Fig. 5).

We then checked if CON1 and CON2 could create nanoparticles on their own. Our results from the Zetasizer showed that both CON1 and CON2 had uniform nanoparticle sizes around 180 nm with a low polydispersity index of less than 0.2 (Table 2, Fig. 6A). The positive zeta potential above 20 indicated that larger aggregates were unlikely to form (Table 2). We also used chemical modeling to predict if CON1 and

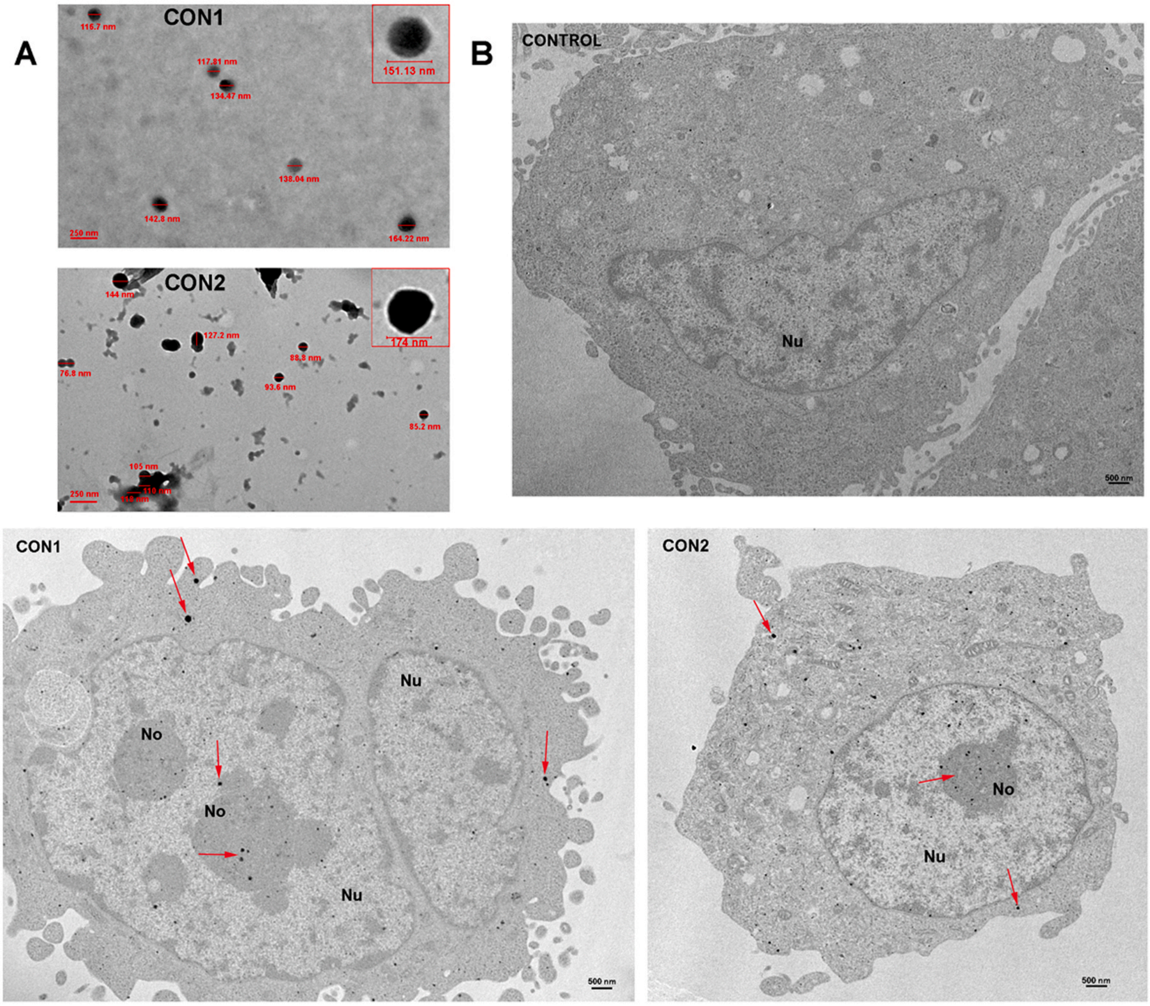

Fig. 7. TEM characterization and intracellular localization of CON1 and CON2. (**A**) The size and shape of nanoparticles obtained using TEM with a digital camera SIS MegaView III and iTEM software. (**B**) The cellular import and subcellular distribution of 5 μM CON1 and CON2 in U87 cells after 24 h treatment. The nucleus is abbreviated as "Nu" and the nucleolus as "No". The scale bar is 500 nm.

CON2 could fold spontaneously like proteins (Fig. 6B). We found that the strong intramolecular forces made CON1 and CON2 fold spontaneously. We also predicted the pKa for CON1 and CON2, which showed that both molecules have protonated aliphatic nitrogen under certain conditions. We then used these structures for conformational search to find stable structures in solution. The most stable conformers for both molecules showed several intramolecular H-bonds and additional hydrophobic interactions. Some of the functional groups (–OH, amide, –NH_2^+–) and hydrophobic structures can be used for further supramolecular organization (Fig. 6B).

The formation of CON1 and CON2 nanoparticles was also confirmed by TEM (Fig. 7). Different sizes of nanoparticles were detected, ranging from 116.7 nm to 164.2 nm for CON1 and 76.8 nm to 174 nm for CON2 (Fig. 7A). Moreover, the TEM revealed that 5 μM of CON1 and CON2 can penetrate U87 glioblastoma cells and can be found in various parts of the cell such as cytoplasm, cellular membrane, nuclear membrane, mitochondrial membranes, nucleus, and nucleolus. Control micrographs of untreated cells were also assessed (Fig. 7B).

3.5. *The effects of CON1and CON2 on DNA damage induction*

We compared the impact of CON1 and CON2 on DNA damage induction with that of DOX, an anticancer drug that primarily causes DNA breaks. To assess DNA damage in U87 and U87-TxR cells, we measured the expression levels of pH2A.X histone, a DNA double-stranded breaks marker, after treating the cells with 2, 5, 10, and 20 μM of DOX, CON1, or CON2 for 24 h. Our results showed that DOX caused significant DNA damage in both U87 and U87-TxR cells, with a more prominent effect on U87 cells (Fig. 8). On the other hand, CON1 and CON2 significantly increased pH2A.X expression at 20 μM in both glioblastoma cell lines. The CON2 effect was also significant at 10 μM in U87-TxR cells (Fig. 8).

3.6. *The effects of CON1 and CON2 on oxidative stress*

We conducted flow cytometry analyses using DHE, DHR, and JC-1 staining to investigate the effects of DOX, CON1, and CON2 at 2 μM on oxidative stress in U87 glioblastoma cells after 24 h. Our findings revealed that all three compounds increased the levels of superoxide anion O_2^-(Fig. 9A), hydrogen peroxide H_2O_2, and peroxynitrite $ONOO^-$ (Fig. 9B) in U87 cells. These increases were determined through DHE and DHR-activated fluorescence. DOX treatment significantly affected mitochondrial membrane potential, as evidenced by JC-1 ratiometric dye, with more than 60% depolarization compared to untreated control cells, while the effects of CON1 and CON2 were less prominent (Fig. 9C).

We also performed a mitochondrial stress test to analyze mitochondrial respiration by treating U87 cells with 5 μM DOX or CON1 for 24 h before measuring the oxygen consumption rate (OCR) using the Sea-Horse XF HS Mini Analyzer (Fig. 9D). The OCR was measured after treatment with oligomycin, FCCP, and rotenone & antimycin A. Using these modulators, we were able to calculate non-mitochondrial

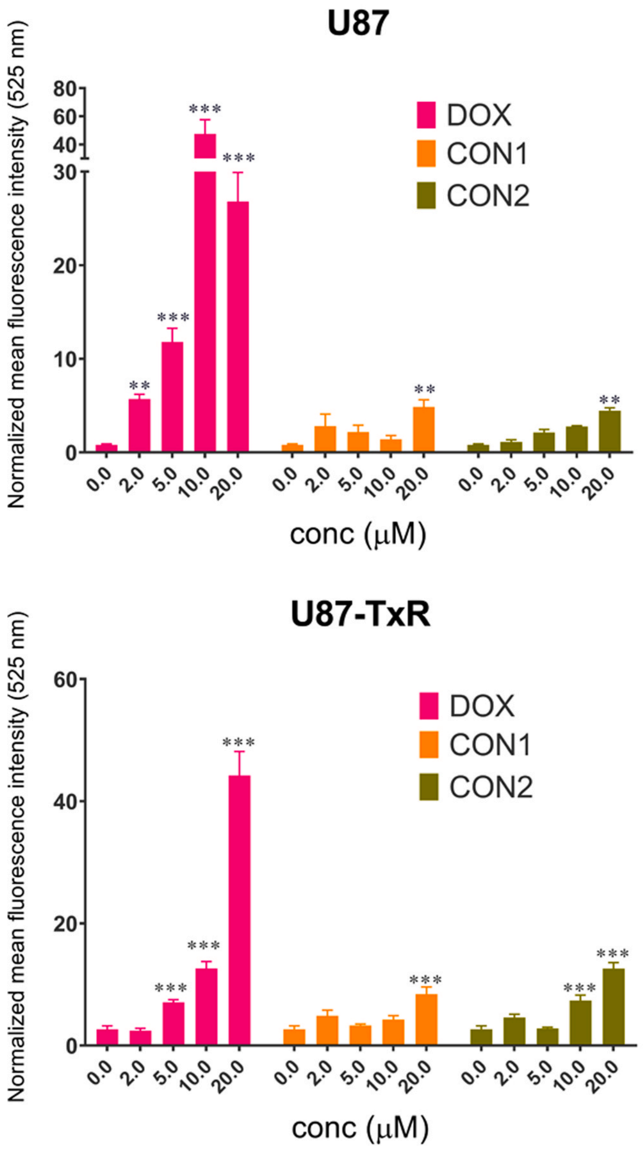

Fig. 8. DNA damage induction by DOX, CON1, and CON2 in U87 and U87-TxR glioblastoma cells. The level of DNA damage was determined by measuring the expression of pH2A.x in U87 and U87-TxR cells. The cells were exposed to different concentrations of DOX, CON1 and CON2 (2, 5, 10 and 20 μM) for 24 h, and then pH2A.x antibody was used to label the cells. The mean fluorescence intensity at 525 nm was measured using flow cytometry. CytExpert software was utilized to identify viable cells and normalize the average mean fluorescence per cell. The results were statistically analyzed using GraphPad Prism 8.0.2 software with a Two-way ANOVA test (Dunnett's multiple comparisons test). The analysis revealed a significant difference between treated and untreated samples, which is represented as $^{**}p \leq 0.01$ and $^{***}p \leq 0.001$.

respiration, basal respiration, maximal respiration, proton leak, ATP production, and spare capacity. Our results indicated that DOX treatment resulted in a significant decrease in basal respiration, maximal respiration, ATP production, and spare capacity, while the effect of CON1 did not differ significantly from the untreated control (Fig. 9D).

3.7. Cell death induction and cell cycle disturbance in ASC patient-derived cells upon treatment with CON1 and CON2

We studied the induction of cell death in ASC cells by DOX, CON1, and CON2 after 72 h, using flow cytometry analysis of AV/PI staining (Fig. 10A, B). We also evaluated cell cycle disturbance using PI staining of ASC cells' DNA after 48 h (Fig. 10C, D). Our findings revealed that the novel hybrids (CON1 and CON2) induced early and late apoptosis, with CON2 showing a more pronounced effect, whereas DOX induced necrosis and late apoptosis (Fig. 10A). The histograms presented in Fig. 10B support our observations. Furthermore, all the compounds disrupted the cell cycle of ASC cells (Fig. 10C). The control sample showed slow progression through the cell cycle, with almost all viable cells in the G0/G1 phase (Fig. 10C). However, CON1 and CON2 notably shifted cells towards the G2/M phase. The corresponding histograms are presented in Fig. 10D.

3.8. The effects of CON1 on cell cycle disturbance and senescence

We examined the effects of 2 μM DOX and 2 and 20 μM CON1 on the cell cycle disturbance in the U87 cell line. Our findings show that 2 μM DOX caused a significant shift of U87 cells to the G2/M phase and doubled the percentage of cells in the subG0 phase (Fig. 11A and B). CON1 at the same concentration resulted in an even higher number of cells in the G2/M phase (Fig. 11A and B). When treated with 20 μM CON1, U87 cells shifted entirely towards polyploidy (Fig. 11A).

We also assessed the potential of DOX and CON1 to induce senescence in U87 cells. By measuring β-galactosidase activity through flow cytometry, we found that CON1 treatment significantly increased the number of U87 cells metabolizing FDG (Fig. 11C and D). Specifically, 2 μM and 20 μM treatments resulted in approximately 23% and 65% FDG-positive cells, respectively (Fig. 11C and D). However, cellular senescence was not evident after DOX treatment (Fig. 11C and D).

4. Discussion

The treatment of glioblastoma faces significant obstacles, such as the presence of the BBB, which prevents potent anticancer drugs from entering the brain and attacking glioblastoma cells, including natural compounds such as DOX [21], and the heterogeneity of glioblastoma, which promotes the development of therapy resistance [40]. Although DOX is a potent anticancer drug, the development of resistance and its side effects are significant drawbacks to its application. Numerous studies have attempted to establish DOX as a valuable anti-glioblastoma drug by testing different combinations of DOX with other anticancer agents [41–44] and delivering it using various nanoparticles [45–47]. Moreover, modifying the structure of DOX is considered a potential solution since DOX comprises two active sites (–NH_2 and –OH), making it a suitable candidate for modification, so other authors have reported the hybridization of DOX with different pharmacophores [48]. Our study presents a novel approach by creating hybrid compounds (CON1 and CON2) that incorporate DOX through modification at –NH_2. These compounds feature a distinctive structure consisting of highly lipophilic SC [1] and highly hydrophobic DOX [49]. These hybrid compounds have the unique ability to form nanoparticles spontaneously and merit further investigation due to their advantageous features, reduced resistance, and improved selectivity compared to DOX.

In our research, we analyzed the impact of SC on various cancer cell lines, including both sensitive and MDR colorectal carcinoma, NSCLC, and glioblastoma cells. Interestingly, we discovered that SC only showed collateral sensitivity in a particular pair of sensitive and MDR glioblastoma cells. After conducting SwissADME analysis, we determined that SC could cross the BBB and was not a substrate of the P-gp, which is a component of the BBB and can be located on the membrane of cancer MDR cells. P-gp plays a critical role in extruding various anticancer drugs [50]. As a result, we thought that combining SC with DOX might be beneficial in sensitizing cancer cells. We observed a synergistic relationship between SC and DOX, which depended on the cell type. The synergism mainly occurred in MDR NSCLC NCI-H460/R and glioblastoma U87-TxR cell lines, with synergistic interaction also observed in another glioblastoma U251 cell line. Significantly, when combined with DOX, SC produced a pronounced antagonism in normal fibroblasts

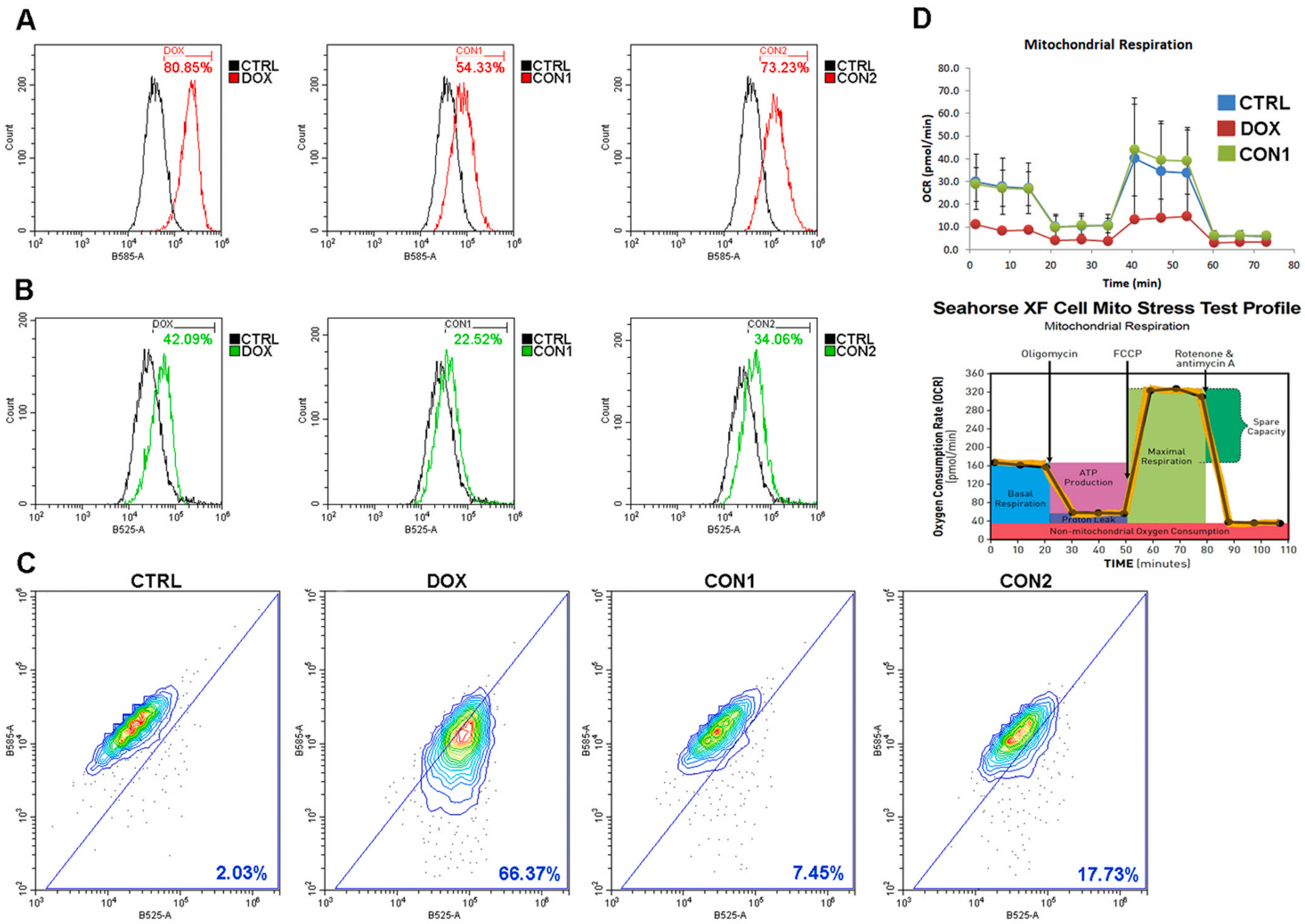

Fig. 9. Oxidative stress induced by DOX, CON1, and CON2 in U87 glioblastoma cell line. (**A**) The levels of superoxide anion (O_2) were measured using DHE after 24 h of treatment with 2 μM DOX, CON1, and CON2; (**B**) the production of hydrogen peroxide (H_2O_2) and peroxynitrite ($ONOO^-$) was evaluated using DHR; (**C**) changes in the mitochondrial membrane potential were assessed by JC-1 using flow cytometry. The results were analyzed by CytExpert software, and each sample was assessed for at least 10,000 events. Representative flow cytometry graphs and plots are presented. (**D**) U87 cells were subjected to a treatment of 5 μM DOX and CON1, and were then metabolically profiled using the Mito Stress Test Profile on the Seahorse XF HS Mini Analyzer. The mitochondrial oxygen consumption curves are presented as averages, with standard deviations shown for each measurement time point (n = 9). The initial three measurement points represent basal mitochondrial respiration. The next three points, after blocking adenine nucleotide translocating by adding oligomycin, represent proton leak-stimulated oxygen consumption. The following three points represent maximal mitochondrial oxygen consumption capacity when the mitochondrial inner membrane is uncoupled by FCCP. The last three points are for non-mitochondrial oxygen consumption when the mitochondrial respiratory chain is inhibited by rotenone and antimycin A. The results were analyzed by the Wave Pro software.

MRC-5, indicating that SC modulated DOX activity to improve its selectivity towards cancer cells. In sensitive NSCLC NCI-H460 and glioblastoma U87 cell lines, the interaction between SC and DOX was additive, signifying better efficacy in cancer MDR cells. However, the interaction was antagonistic in both sensitive DLD1 and multidrug-resistant DLD1-TxR colorectal carcinoma cell lines, indicating a cell type-dependent effect of SC on DOX activity. Our additional DOX accumulation study confirmed these findings, as SC increased DOX accumulation in MDR NSCLC NCI-H460 and glioblastoma U87-TxR cells, as well as two other glioblastoma cell lines, U87 and U251. However, we did not observe any increase in DOX accumulation in colorectal carcinoma cells or sensitive NSCLC cells.

Next, we explored the development of a hybrid compound consisting of SC and DOX. We were encouraged by promising literature results that showed strong anticancer activities *in vivo* with lipid nanoparticles co-delivering SC and DOX [33]. To investigate the synergistic effects of low concentrations of SC, we tested different ratios of SC:DOX (1:1, 2:1, and 5:1) on glioblastoma U87 and U87-TxR cells in the nanomolar range. We found a synergistic interaction, which prompted us to pursue our endeavor. To create our compounds, CON1 and CON2, we used linkers that cannot be hydrolyzed in physiological conditions, also ensuring the preservation of DOX fluorescence for accumulation and localization studies. The only difference between CON1 and CON2 is the length of the linker between SC and DOX. We also explored the anticancer effects of SC derivatives LIG1 and LIG2, which form CON1 and CON2, respectively. LIG1 and LIG2 had even poorer effects on glioblastoma U87 and U87-TxR cells than SC, but both preserved the collateral sensitivity characteristic of SC. On the other hand, the IC_{50} values for CON1 and CON2 were significantly lower than the IC_{50} value for SC in U87 cells, but they did not preserve collateral sensitivity. Although U87-TxR cells were resistant to CON1 and CON2, the resistances were significantly lower than the resistance to DOX. Importantly, the selectivity of both CON1 and CON2 towards glioblastoma cells was considerably increased compared to SC or DOX alone. Our findings indicate that CON1 and CON2 show improved anticancer properties over DOX.

To compare the effectiveness of our hybrid compounds and DOX with TMZ, the only available chemotherapeutic for primary brain tumors of glial origin [51], we conducted experiments on astrocytoma grade 3 patient-derived cells. We wanted to determine if the anticancer

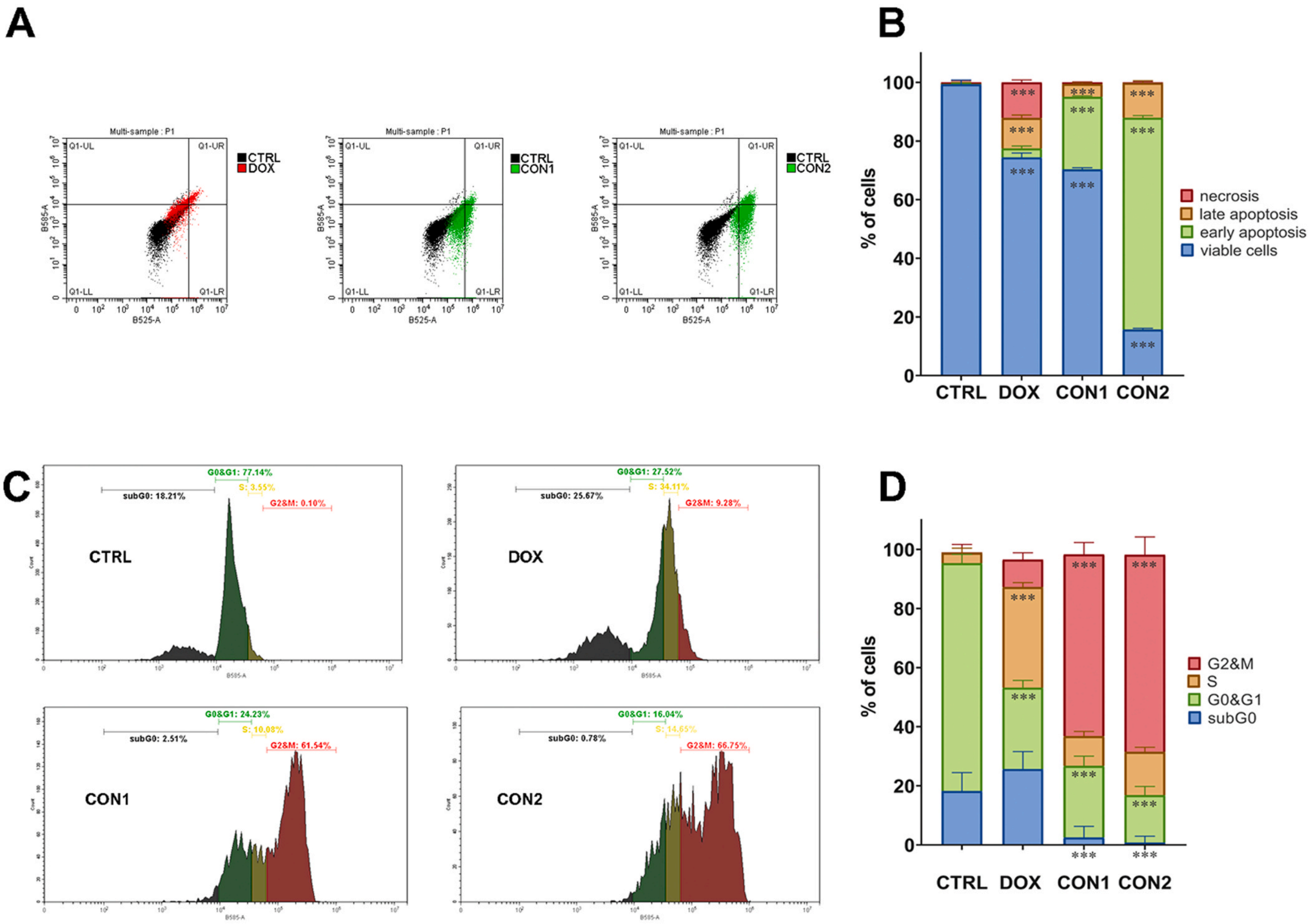

Fig. 10. Cell death and cell cycle analyses in primary ASC cells upon treatment with DOX, CON1 and CON2. The cells were treated with 1 μM DOX and 10 μM CON1 and CON2. (**A**) The cell death induction assessed by AV/PI staining after 72 h of treatment (overlaid dot plots) were evaluated by flow cytometry and analyzed using CytExpert software. Representative flow cytometry plots are presented. (**B**) The percentages of viable (AV- PI-), early apoptotic (AV+ PI-), late apoptotic (AV+ PI+), and necrotic (AV- PI+) cells are illustrated in a histogram. At least 10,000 events were collected for each experimental sample. (**C**) The cell cycle distribution assessed by PI staining after 48 h of treatment were evaluated by flow cytometry and analyzed using CytExpert software. Representative flow cytometry graphs are presented. (**D**) The percentages of cells in different cell cycle phases (subG0, G0/G1, S, and G2/M) are presented in a histogram. At least 10,000 events were collected for each experimental sample. Statistical analysis was performed in GraphPad Prism 8.0.2 using Two-way ANOVA (Dunnett's multiple comparisons test). A statistically significant difference between treated samples and untreated control is shown as ***$p \leq 0.001$.

efficacy was dependent on the initial cell density, so we seeded ASC cells at two different densities. After conducting an end-point assay at time point 72 h, we discovered no significant differences in cases of hybrid compounds and TMZ. However, DOX exhibited a powerful effect within the nanomolar range, exhibiting a nearly 6-fold difference and performing better in ASC cells seeded at a lower density. This finding contrasts recent discoveries in breast cancer cells, which demonstrated reduced accumulation and effectiveness of DOX due to elevated expression levels of ABC transporters at lower initial cell density [52]. While CON1 and CON2 were more active against ASC cells than in MDR U87-TxR cells, they were less active in sensitive U87 cells. Unfortunately, the effect of TMZ was very poor, with an IC_{50} value that exceeded 500 μM. We then assessed the real-time cell growth of ASC cells when treated with five different concentrations of CON1, CON2, DOX, and TMZ. Our findings revealed that the effects of different DOX concentrations were mainly cytotoxic, whereas the effects of CON1 and CON2 were mainly antiproliferative. The concentration near IC_{50} values for the end-point assay (20 μM) was cytostatic, while a higher concentration (50 μM) was cytotoxic. Only the highest concentration of TMZ (500 μM) was cytostatic. These results support the notion that TMZ is relatively ineffective in glioma treatment and suggest that it only exerts cytostatic but not cytotoxic activity [53].

As our hybrid compounds preserved the fluorescence, we utilized this feature to study their localization in glioblastoma cells. It is widely known that DOX localizes primarily in the nucleus, targeting DNA and displaying concentrated fluorescence in the nucleus [54]. Therefore, it was surprising to discover that the fluorescence derived from CON1 and CON2 was peri-nuclear. Upon researching literature for DOX fluorescence peri-nuclear localization, we found that lipid nanoparticles loaded with DOX exhibit the same fluorescence pattern in cells as we observed with CON1 and CON2 [55]. This encouraged us to investigate the nanoparticle nature of our novel hybrid compounds. Zetasizer analysis revealed that CON1 and CON2 form nanoparticles that are characterized by a uniform size of approximately 180 nm and a low polydispersity index below 0.2, which is similar to that observed with purpose-made nanoparticles [56,57]. Additionally, positive zeta potential above 20 indicated that larger aggregates were unlikely to form. Chemical modeling showed that both CON1 and CON2 single molecules spontaneously fold in a 'protein-like' manner and predict their packing in larger forms, such as nanoparticles. We confirmed the presence of nanoparticles derived from CON1 and CON2 by TEM, also used to evaluate their intracellular localization. Our hybrid compounds were found in various cellular compartments, including the cytoplasm, cellular membrane, nuclear membrane, mitochondrial membranes,

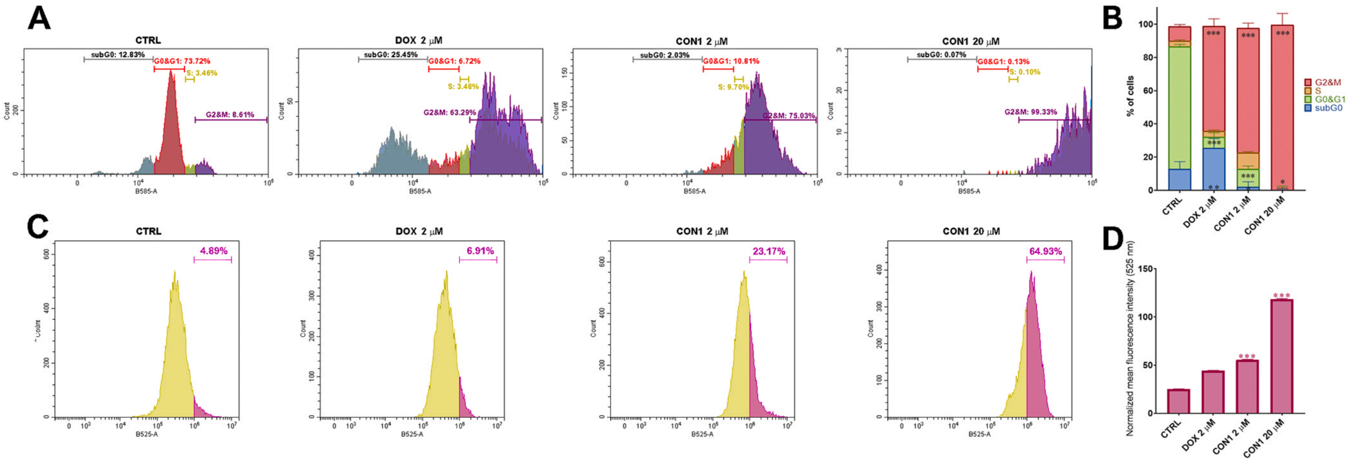

Fig. 11. Cell cycle and senescence assessment in U87 glioblastoma cell line upon treatment with DOX and CON1. The cells were subjected to treatment with 2 μM DOX, as well as 2 and 20 μM CON1. (**A**) The cell cycle distribution was assessed after 48 h of treatment using PI staining and analyzed using the CytExpert software. Representative flow cytometry graphs are presented. (**B**) The percentages of cells in different cell cycle phases (subG0, G0/G1, S, and G2/M) are presented in a histogram. At least 10,000 events were collected for each experimental sample. (**C**) β-galactosidase activity was evaluated using FDG after 72 h of treatment, and the results were analyzed by CytExpert software. The number of FDG positive cells was presented as percentages in an arbitrary set gate within the representative flow cytometry graphs. (**D**) The mean FDG fluorescence intensity at 525 nm was measured using flow cytometry. CytExpert software was used to identify viable cells and normalize the average mean FDG fluorescence per cell. Statistical analysis was performed in GraphPad Prism 8.0.2 using Two-way ANOVA (Dunnett's multiple comparisons test). A statistically significant difference between treated samples and untreated control is presented as $^*p \leq 0.05$, $^{**}p \leq 0.01$ and $^{***}p \leq 0.001$.

nucleus, and nucleolus. This indicates that CON1 and CON2 can enter the nucleus, albeit to a lesser extent than DOX, and as such, their fluorescence cannot be detected in the nucleus. Our hybrids may elicit molecular mechanisms similar to DOX but with a prolonged yet less cytotoxic effect due to the lack of preferential accumulation in the nucleus. Consequently, we compared the impacts of DOX, CON1, and CON2 on several cellular processes.

DOX acts by inhibiting or poisoning topoisomerase IIα, intercalating into DNA, causing DNA damage, generating free radicals, and leading to oxidative stress, which results in its cytotoxic effects [58]. Therefore, we tested the impact of increasing DOX, CON1, and CON2 concentrations on inducing DNA damage in glioblastoma cells. After 24 h of treatment, we found that DOX caused significantly more DNA damage than CON1 and CON2. Additionally, DOX was found to be more effective in sensitive than in MDR glioblastoma cells. On the other hand, CON1 and CON2 had similar effects on DNA in both types of glioblastoma cells, regardless of their MDR phenotype. Notably, CON2 had a more pronounced effect on MDR glioblastoma cells than on sensitive ones. As DNA damage can be caused by reactive oxygen and nitrogen species generation, we also examined the effects of DOX, CON1, and CON2 on the levels of superoxide anion $O_2^{\bar{}}$, hydrogen peroxide H_2O_2, and peroxynitrite $ONOO^-$ after 24 h. We discovered that all the compounds significantly increased ROS and RNS levels in glioblastoma cells. The effect was more pronounced in the case of ROS. This led us to investigate the possible impact on mitochondrial membrane potential and mitochondrial respiration. Our findings showed that DOX caused mitochondrial damage, reflected in membrane depolarization and impaired respiration. We did not observe this effect with the hybrid compounds. Specifically, CON1 caused no change in the oxygen consumption rate over time, similar to that of the untreated control cells.

Our results suggest that hybrids may cause less harm to cells than DOX. This may be attributed to their degradation/stability ratio within the cell and slower release of DOX, as our research showed that nanoparticles were present in nearly all cellular structures after 24 h of treatment. The effectiveness and safety of active hybrid molecules may depend on their degradation, which can occur through hydrolytic or oxidative pathways [59]. Our hybrids, which contain an amide linker, exhibit hydrolytic stability [60–62]. Therefore, oxidative degradation may be a more feasible mechanism for our hybrids in the intracellular environment. This could be advantageous, as cancer cells typically experience higher levels of oxidative stress than normal cells [63], potentially contributing to the selectivity of hybrids towards cancer cells due to a more dynamic release of DOX in cancer than in normal cells. Even more, amide-linked daunorubicin analogues have been found to be less toxic to healthy cells compared to analogues linked with an amine spacer [64]. Although hybrids with amide linker shows lower anticancer activity, this approach shows promise for safer and more effective cancer treatment.

Observed oxidative stress induced by DOX, CON1, and CON2 could be followed by cell death induction and changed cell cycle progression. Some findings linked the increase in ROS with the polyploidization of cells [65]. Our research revealed that DOX and hybrid compounds significantly influenced ASC patient-derived and U87 cells, by accumulating them in the G2/M phase. DOX induced late apoptosis and necrosis in ASC cells, whereas CON1 and CON2 predominantly triggered early apoptosis. In the case of U87 cells treated with CON1, we suspected polyploidization and complete absence of cell cycle progression at a concentration of 20 μM. Upon this, we explored whether CON1 had the ability to trigger senescence in U87 cells. Our investigation revealed that glioblastoma cells treated with CON1 had a significant increase in the activity of β-galactosidase, an enzyme associated with senescence [66]. Senescence and apoptosis are two separate processes that can result in cell death and inhibit tumor growth [67]. Typically, senescent cells are resistant to apoptosis [68]. Hence, our findings were interesting since CON1 induced apoptosis in ASC cells and senescence in U87 cells. Nonetheless, it is possible for the same drug to elicit different mechanisms of cell death in distinct cells. For instance, the effect of DOX on apoptosis, necrosis, autophagy, or senescence is depending on factors like cell and cancer type, DOX concentration, and treatment duration [69].

Inhibiting Mdm2 through nucleolar (ribosome biosynthesis disturbance) and oxidative stress may activate p53-dependent anticancer pathways [70]. This activation leads to an increase in p53 levels, stabilization, and ultimately, apoptosis, autophagy, senescence, metabolic changes, cell cycle arrest, or DNA repair. TEM imaging has revealed our hybrids within the nucleolus, which may impact nucleolus function. Besides, CON1 and CON2 induce oxidative stress and G2/M arrest. Therefore, the anticancer effect of hybrids could be linked to p53 activation, given that U87 and ASC have wild-type p53. However, further comparative studies using cellular models with both wild-type and mutated p53 are necessary to confirm this hypothesis.

5. Conclusion

Our study showed that hybrid compounds of doxorubicin and the natural compound sclareol may be a promising strategy to overcome the limitations of doxorubicin application for cancer patients. Our hybrid compounds, CON1 and CON2, which spontaneously form nanoparticles, showed improved anticancer properties compared to doxorubicin, with increased selectivity and reduced resistance. However, further research is necessary to determine the optimal dosage and administration of the hybrid compounds and their potential adverse effects *in vivo*. Studies are underway to investigate whether CON1 and CON2 can cross the BBB and to compare the cardiotoxic effects of doxorubicin and hybrid compounds. Although our study has limitations, we are confident that the results provide valuable insights. It is important to note that we did not include a tumor-bearing animal experiment to definitively determine the hybrids' effectiveness. Despite being an *in vitro* study, we have included a patient primary cell culture in our research, which enhances the validity of our findings. While our investigation focuses on the physicochemical properties and effects of hybrid compounds on glioblastoma cells, we are confident that our study paves the way for further preclinical studies in this area.

CRediT authorship contribution statement

Ana Stepanović: Writing – original draft, Investigation. **Aleksandra Korać:** Investigation, Formal analysis. **Nataša Terzić Jovanović:** Investigation. **Igor Nikolić:** Investigation. **Mario Zlatović:** Investigation. **Igor Opsenica:** Supervision, Conceptualization. **Milica Pešić:** Writing – review & editing, Supervision, Funding acquisition, Conceptualization.

Declaration of Competing Interest

The authors declare the following financial interests/personal relationships which may be considered as potential competing interests: MP, AS, IO, and NTJ are inventors on a patent application HYBRID COMPOUNDS OF SCLAREOL AND DOXORUBICIN, THEIR SYNTHESIS AND APPLICATION, Priority date: November 14th, 2022, PCT Application No: PCT/RS2023/000016

Data availability

Data will be made available on request.

Acknowledgement

This research was funded by the Ministry of science, technological development and innovation of the Republic of Serbia, grant numbers (451–03–47/2023–01/200007 and 451–03–47/2023–01/200168) and by Proof of Concept internal project SclarDoxInn at the Institute for Biological Research "Siniša Stanković" - National Institute of the Republic of Serbia, University of Belgrade, funded by Serbia Accelerating Innovation and Growth Entrepreneurship (SAIGE) World Bank Program.

Appendix A. Supporting information

Supplementary data associated with this article can be found in the online version at doi:10.1016/j.biopha.2024.116496.

References

[1] J. Zhou, X. Xie, H. Tang, C. Peng, F. Peng, The bioactivities of sclareol: a mini review, Front Pharm. *13* (2022) 1014105, https://doi.org/10.3389/fphar.2022.1014105.

[2] I. Sartori Tamburlin, E. Roux, M. Feuillee, J. Labbe, Y. Aussagues, F.E. El Fadle, F. Fraboul, G. Bouvier, Toxicological safety assessment of essential oils used as food supplements to establish safe oral recommended doses, Food Chem. Toxicol. *157* (2021) 112603, https://doi.org/10.1016/j.fct.2021.112603.

[3] K. Dimas, D. Kokkinopoulos, C. Demetzos, B. Vaos, M. Marselos, M. Malamas, T. Tzavaras, The effect of sclareol on growth and cell cycle progression of human leukemic cell lines, Leuk. Res *23* (1999) 217–234, https://doi.org/10.1016/s0145-2126(98)00134-9.

[4] K. Dimas, C. Demetzos, V. Vaos, P. Ioannidis, T. Trangas, Labdane type diterpenes down-regulate the expression of c-Myc protein, but not of Bcl-2, in human leukemia T-cells undergoing apoptosis, Leuk. Res *25* (2001) 449–454, https://doi.org/10.1016/s0145-2126(00)00150-8.

[5] K. Dimas, S. Hatziantoniou, S. Tseleni, H. Khan, A. Georgopoulos, K. Alevizopoulos, J.H. Wyche, P. Pantazis, C. Demetzos, Sclareol induces apoptosis in human HCT116 colon cancer cells in vitro and suppression of HCT116 tumor growth in immunodeficient mice, Apoptosis *12* (2007) 685–694, https://doi.org/10.1007/s10495-006-0026-8.

[6] J.W. Mo, R.Z. Yang, D.F. Zhang, Modulation of anoikis resistance in MG63 osteosarcoma cells by sclareol via inhibiting Ezrin/Fak expression, Int. J. Clin. Exp. Pathol. *9* (2016) 6795–6803. ISSN:1936-2625/IJCEP0021321.

[7] T. Zhang, T. Wang, P. Cai, Sclareol inhibits cell proliferation and sensitizes cells to the antiproliferative effect of bortezomib via upregulating the tumor suppressor caveolin-1 in cervical cancer cells, Mol. Med Rep. *15* (2017) 3566–3574, https://doi.org/10.3892/mmr.2017.6480.

[8] H.L. Chen, J.Y. Gong, S.C. Lin, S. Li, Y.C. Chiang, J.H. Hung, C.C. Yen, C.C. Lin, Effects of sclareol against small cell lung carcinoma and the related mechanism: in vitro and in vivo studies, Anticancer Res. *40* (2020) 4947–4960, https://doi.org/10.21873/anticanres.14498.

[9] H. Wang, M. Xie, G. Rizzi, X. Li, K. Tan, M. Fussenegger, Identification of sclareol as a natural neuroprotective Ca(v) 1.3-antagonist using synthetic parkinson-mimetic gene circuits and computer-aided drug discovery, Adv. Sci. (Weinh.) *9* (2022) e2102855, https://doi.org/10.1002/advs.202102855.

[10] P. Stojkovic, A. Kostic, E. Lupsic, N.T. Jovanovic, M. Novakovic, P. Nedialkov, A. Trendafilova, M. Pesic, I.M. Opsenica, Novel hybrids of sclareol and 1,2,4-triazolo[1,5-a]pyrimidine show collateral sensitivity in multidrug-resistant glioblastoma cells, Bioorg. Chem. *138* (2023) 106605, https://doi.org/10.1016/j.bioorg.2023.106605.

[11] J. Ahmed II, A.A. Abdul Hamid, K.B. Abd Halim, A.T. Che Has, P-glycoprotein: new insights into structure, physiological function, regulation and alterations in disease, Heliyon *8* (2022) e09777, https://doi.org/10.1016/j.heliyon.2022.e09777.

[12] C.F. Thorn, C. Oshiro, S. Marsh, T. Hernandez-Boussard, H. McLeod, T.E. Klein, R. B. Altman, Doxorubicin pathways: pharmacodynamics and adverse effects, Pharm. Genom. *21* (2011) 440–446, https://doi.org/10.1097/FPC.0b013e32833ffb56.

[13] L. Zhu, M. Lin, The Synthesis of Nano-Doxorubicin and its Anticancer Effect, Anticancer Agents Med Chem. *21* (2021) 2466–2477, https://doi.org/10.2174/1871520621666201229115612.

[14] N. Seebacher, D.J. Lane, D.R. Richardson, P.J. Jansson, Turning the gun on cancer: Utilizing lysosomal P-glycoprotein as a new strategy to overcome multi-drug resistance, Free Radic. Biol. Med *96* (2016) 432–445, https://doi.org/10.1016/j.freeradbiomed.2016.04.201.

[15] S.R. Lin, C.H. Chang, C.F. Hsu, M.J. Tsai, H. Cheng, M.K. Leong, P.J. Sung, J. C. Chen, C.F. Weng, Natural compounds as potential adjuvants to cancer therapy: preclinical evidence, Br. J. Pharm. *177* (2020) 1409–1423, https://doi.org/10.1111/bph.14816.

[16] P.S. Rawat, A. Jaiswal, A. Khurana, J.S. Bhatti, U. Navik, Doxorubicin-induced cardiotoxicity: an update on the molecular mechanism and novel therapeutic strategies for effective management, Biomed. Pharm. *139* (2021) 111708, https://doi.org/10.1016/j.biopha.2021.111708.

[17] Z. Xie, M. Chen, J. Lian, H. Wang, J. Ma, Glioblastoma-on-a-chip construction and therapeutic applications, Front Oncol. *13* (2023) 1183059, https://doi.org/10.3389/fonc.2023.1183059.

[18] K. Szklener, M. Mazurek, M. Wieteska, M. Waclawska, M. Bilski, S. Mandziuk, New DIrections in the Therapy of Glioblastoma, Cancers (Basel) *14* (2022), https://doi.org/10.3390/cancers14215377.

[19] A.C. Tan, D.M. Ashley, G.Y. Lopez, M. Malinzak, H.S. Friedman, M. Khasraw, Management of glioblastoma: State of the art and future directions, CA Cancer J. Clin. *70* (2020) 299–312, https://doi.org/10.3322/caac.21613.

[20] M.M. Kim, Y. Umemura, D. Leung, Bevacizumab and glioblastoma: past, present, and future directions, Cancer J. *24* (2018) 180–186, https://doi.org/10.1097/PPO.0000000000000326.

[21] D. Wang, C. Wang, L. Wang, Y. Chen, A comprehensive review in improving delivery of small-molecule chemotherapeutic agents overcoming the blood-brain/brain tumor barriers for glioblastoma treatment, Drug Deliv. *26* (2019) 551–565, https://doi.org/10.1080/10717544.2019.1616235.

[22] J.V. Gregory, P. Kadiyala, R. Doherty, M. Cadena, S. Habeel, E. Ruoslahti, P. R. Lowenstein, M.G. Castro, J. Lahann, Systemic brain tumor delivery of synthetic protein nanoparticles for glioblastoma therapy, Nat. Commun. *11* (2020) 5687, https://doi.org/10.1038/s41467-020-19225-7.

[23] S. Wohlfart, A.S. Khalansky, S. Gelperina, O. Maksimenko, C. Bernreuther, M. Glatzel, J. Kreuter, Efficient chemotherapy of rat glioblastoma using doxorubicin-loaded PLGA nanoparticles with different stabilizers, PLoS One *6* (2011) e19121, https://doi.org/10.1371/journal.pone.0019121.

[24] C.P. Beier, C. Schmid, T. Gorlia, C. Kleinletzenberger, D. Beier, O. Grauer, A. Steinbrecher, B. Hirschmann, A. Brawanski, C. Dietmaier, et al., RNOP-09: pegylated liposomal doxorubicine and prolonged temozolomide in addition to

radiotherapy in newly diagnosed glioblastoma–a phase II study, BMC Cancer *9* (2009) 308, https://doi.org/10.1186/1471-2407-9-308.

[25] J.R. Whittle, J.D. Lickliter, H.K. Gan, A.M. Scott, J. Simes, B.J. Solomon, J. A. MacDiarmid, H. Brahmbhatt, M.A. Rosenthal, First in human nanotechnology doxorubicin delivery system to target epidermal growth factor receptors in recurrent glioblastoma, J. Clin. Neurosci.: Off. J. Neurosurg. Soc. Australas. *22* (2015) 1889–1894, https://doi.org/10.1016/j.jocn.2015.06.005.

[26] B. Kasenda, D. Konig, M. Manni, R. Ritschard, U. Duthaler, E. Bartoszek, A. Barenwaldt, S. Deuster, G. Hutter, D. Cordier, et al., Targeting immunoliposomes to EGFR-positive glioblastoma, ESMO Open *7* (2022) 100365, https://doi.org/10.1016/j.esmoop.2021.100365.

[27] https://clinicaltrials.gov/study/NCT02372409.

[28] E.C. Leuthardt, C. Duan, M.J. Kim, J.L. Campian, A.H. Kim, M.M. Miller-Thomas, J. S. Shimony, D.D. Tran, Hyperthermic Laser Ablation of Recurrent Glioblastoma Leads to Temporary Disruption of the Peritumoral Blood Brain Barrier, PloS One *11* (2016) e0148613, https://doi.org/10.1371/journal.pone.0148613.

[29] https://clinicaltrials.gov/study/NCT05864534

[30] K. Dimas, M. Papadaki, C. Tsimplouli, S. Hatziantoniou, K. Alevizopoulos, P. Pantazis, C. Demetzos, Labd-14-ene-8,13-diol (sclareol) induces cell cycle arrest and apoptosis in human breast cancer cells and enhances the activity of anticancer drugs, Biomed. Pharm. *60* (2006) 127–133, https://doi.org/10.1016/j.biopha.2006.01.003.

[31] F. Perche, V.P. Torchilin, Cancer cell spheroids as a model to evaluate chemotherapy protocols, Cancer Biol. Ther. *13* (2012) 1205–1213, https://doi.org/10.4161/cbt.21353.

[32] M.S. Oliveira, B.H.S. Lima, G.A.C. Goulart, S.V. Mussi, G.S.M. Borges, R.L. Orefice, L.A.M. Ferreira, Improved Cytotoxic Effect of Doxorubicin by Its Combination with Sclareol in Solid Lipid Nanoparticle Suspension, J. Nanosci. Nanotechnol. *18* (2018) 5609–5616, https://doi.org/10.1166/jnn.2018.15418.

[33] G.S.M. Borges, J.O. Silva, R.S. Fernandes, A.M. de Souza, G.D. Cassali, M. I. Yoshida, E.A. Leite, A.L.B. de Barros, L.A.M. Ferreira, Sclareol is a potent enhancer of doxorubicin: evaluation of the free combination and co-loaded nanostructured lipid carriers against breast cancer, Life Sci. *232* (2019) 116678, https://doi.org/10.1016/j.lfs.2019.116678.

[34] Pešić, M.; Kostić, A.; Opsenica, I.; Terzić-Jovanović, N. HYBRID COMPOUNDS OF SCLAREOL AND DOXORUBICIN, THEIR SYNTHESIS AND APPLICATION. Priority date: November 14th, 2022, PCT Application No: PCT/RS2023/000016.

[35] A. Podolski-Renic, T. Andelkovic, J. Bankovic, N. Tanic, S. Ruzdijic, M. Pesic, The role of paclitaxel in the development and treatment of multidrug resistant cancer cell lines, Biomed. Pharm. *65* (2011) 345–353, https://doi.org/10.1016/j.biopha.2011.04.015.

[36] M. Pesic, J.Z. Markovic, D. Jankovic, S. Kanazir, I.D. Markovic, L. Rakic, S. Ruzdijic, Induced resistance in the human non small cell lung carcinoma (NCI-H460) cell line in vitro by anticancer drugs, J. Chemother. *18* (2006) 66–73, https://doi.org/10.1179/joc.2006.18.1.66.

[37] A. Daina, O. Michielin, V. Zoete, SwissADME: a free web tool to evaluate pharmacokinetics, drug-likeness and medicinal chemistry friendliness of small molecules, Sci. Rep. *7* (2017) 42717, https://doi.org/10.1038/srep42717.

[38] Schrödinger. Schrödinger 1..

[39] Schrödinger2. Schrödinger 2..

[40] Y.A. Yabo, S.P. Niclou, A. Golebiewska, Cancer cell heterogeneity and plasticity: a paradigm shift in glioblastoma, Neuro Oncol. *24* (2022) 669–682, https://doi.org/10.1093/neuonc/noab269.

[41] E.S. Villodre, F.C. Kipper, A.O. Silva, G. Lenz, P. Lopez, Low Dose of Doxorubicin Potentiates the Effect of Temozolomide in Glioblastoma Cells, Mol. Neurobiol. *55* (2018) 4185–4194, https://doi.org/10.1007/s12035-017-0611-6.

[42] C. Baloi, A. Oprita, L.E. Semenescu, D.E. Tache, O.S. Popescu, G.A. Staicu, A. Dricu, Combined effects of doxorubicin and temozolomide in cultured glioblastoma cells, Curr. Health Sci. J. *48* (2022) 263–269, https://doi.org/10.12865/CHSJ.48.03.03.

[43] M. Maszczyk, K. Banach, M. Karkoszka, Z. Rzepka, J. Rok, A. Beberok, D. Wrzesniok, Chemosensitization of U-87 MG Glioblastoma Cells by Neobavaisoflavone towards Doxorubicin and Etoposide, Int J. Mol. Sci. *23* (2022), https://doi.org/10.3390/ijms23105621.

[44] J. Chen, Y.D. Zhuang, Q. Zhang, S. Liu, B.B. Zhuang, C.H. Wang, R.S. Liang, Exploring the mechanism of cordycepin combined with doxorubicin in treating glioblastoma based on network pharmacology and biological verification, PeerJ *10* (2022) e12942, https://doi.org/10.7717/peerj.12942.

[45] M. Ghaferi, A. Raza, M. Koohi, W. Zahra, A. Akbarzadeh, H. Ebrahimi Shahmabadi, S.E. Alavi, Impact of PEGylated Liposomal Doxorubicin and Carboplatin Combination on Glioblastoma, Pharmaceutics *14* (2022), https://doi.org/10.3390/pharmaceutics14102183.

[46] Z. Chen, C. Wang, T.F. Li, K. Li, Y. Yue, X. Liu, H.Z. Xu, Y. Wen, Q. Zhang, M. Han, et al., Doxorubicin conjugated with nanodiamonds and in free form commit glioblastoma cells to heterodromous fates, Nanomed. (Lond.) *14* (2019) 335–351, https://doi.org/10.2217/nnm-2018-0330.

[47] S. Zhang, X. Jiao, M. Heger, S. Gao, M. He, N. Xu, J. Zhang, M. Zhang, Y. Yu, B. Ding, et al., A tumor microenvironment-responsive micelle co-delivered radiosensitizer Dbait and doxorubicin for the collaborative chemo-radiotherapy of glioblastoma, Drug Deliv. *29* (2022) 2658–2670, https://doi.org/10.1080/10717544.2022.2108937.

[48] S. Peter, S. Alven, R.B. Maseko, B.A. Aderibigbe, Doxorubicin-Based hybrid compounds as potential anticancer agents: a review, Molecules *27* (2022), https://doi.org/10.3390/molecules27144478.

[49] H. Zhao, J. Yu, R. Zhang, P. Chen, H. Jiang, W. Yu, Doxorubicin prodrug-based nanomedicines for the treatment of cancer, Eur. J. Med Chem. *258* (2023) 115612, https://doi.org/10.1016/j.ejmech.2023.115612.

[50] J. Dinic, A. Podolski-Renic, M. Jeremic, M. Pesic, Potential of natural-based anticancer compounds for P-glycoprotein inhibition, Curr. Pharm. Des. *24* (2018) 4334–4354, https://doi.org/10.2174/1381612825666190112164211.

[51] M. Willman, J. Willman, J. Figg, E. Dioso, S. Sriram, B. Olowofela, K. Chacko, J. Hernandez, B. Lucke-Wold, Update for astrocytomas: medical and surgical management considerations, Explor Neurosci. *2* (2023) 1–26, https://doi.org/10.37349/en.2023.00009.

[52] S. Shivhare, A. Das, Cell density modulates chemoresistance in breast cancer cells through differential expression of ABC transporters, Mol. Biol. Rep. *50* (2023) 215–225, https://doi.org/10.1007/s11033-022-08028-2.

[53] H. Strobel, T. Baisch, R. Fitzel, K. Schilberg, M.D. Siegelin, G. Karpel-Massler, K. M. Debatin, M.A. Westhoff, Temozolomide and Other Alkylating Agents in Glioblastoma Therapy, Biomedicines *7* (2019), https://doi.org/10.3390/biomedicines7030069.

[54] L. Cui, W. Liu, H. Liu, Q. Qin, S. Wu, S. He, Z. Zhang, X. Pang, C. Zhu, Cascade-targeting of charge-reversal and disulfide bonds shielding for efficient DOX delivery of multistage sensitive MSNs-COS-SS-CMC, Int J. Nanomed. *15* (2020) 6153–6165, https://doi.org/10.2147/IJN.S252769.

[55] N.V. Rusetskaya, N. Khariton, O.V. Yurchenko, V.F. Chekhun, Distribution and accumulation of liposomal form of doxorubicin in breast cancer cells of MCF-7 line, Exp. Oncol. *33* (2011) 78–82.

[56] S. Voci, A. Gagliardi, N. Ambrosio, M.C. Salvatici, M. Fresta, D. Cosco, Gliadin nanoparticles containing doxorubicin hydrochloride: characterization and cytotoxicity, Pharmaceutics *15* (2023), https://doi.org/10.3390/pharmaceutics15010180.

[57] L.B. Macedo, D.R. Nogueira-Librelotto, D. Mathes, J.M. de Vargas, R.M. da Rosa, O. E.D. Rodrigues, M.P. Vinardell, M. Mitjans, C.M.B. Rolim, Overcoming MDR by Associating Doxorubicin and pH-Sensitive PLGA Nanoparticles Containing a Novel Organoselenium Compound-An In Vitro Study, Pharmaceutics *14* (2021), https://doi.org/10.3390/pharmaceutics14010080.

[58] H.L. Ou, R. Hoffmann, C. Gonzalez-Lopez, G.J. Doherty, J.E. Korkola, D. Munoz-Espin, Cellular senescence in cancer: from mechanisms to detection, Mol. Oncol. *15* (2021) 2634–2671, https://doi.org/10.1002/1878-0261.12807.

[59] A.H. Alkhzem, T.J. Woodman, I.S. Blagbrough, Design and synthesis of hybrid compounds as novel drugs and medicines, RSC Adv. *12* (2022) 19470–19484, https://doi.org/10.1039/d2ra03281c.

[60] V.R. Pattabiraman, J.W. Bode, Rethinking amide bond synthesis, Nature *480* (2011) 471–479, https://doi.org/10.1038/nature10702.

[61] S.D. Roughley, A.M. Jordan, The medicinal chemist's toolbox: an analysis of reactions used in the pursuit of drug candidates, J. Med. Chem. *54* (2011) 3451–3479, https://doi.org/10.1021/jm200187y.

[62] D.G. Brown, J. Bostrom, Analysis of Past and Present Synthetic Methodologies on Medicinal Chemistry: Where Have All the New Reactions Gone? J. Med. Chem. *59* (2016) 4443–4458, https://doi.org/10.1021/acs.jmedchem.5b01409.

[63] S. Arfin, N.K. Jha, S.K. Jha, K.K. Kesari, J. Ruokolainen, S. Roychoudhury, B. Rathi, D. Kumar, Oxidative Stress in Cancer Cell Metabolism, Antioxidants *10* (2021), https://doi.org/10.3390/antiox10050642.

[64] A.A. Moiseeva, O.I. Artyushin, L.V. Anikina, V.K. Brel, Synthesis and antitumor activity of daunorubicin conjugates with of 3,4-methylendioxybenzaldehyde, Bioorg. Med. Chem. Lett. *29* (2019) 126617, https://doi.org/10.1016/j.bmcl.2019.08.021.

[65] G. Mosieniak, M.A. Sliwinska, O. Alster, A. Strzeszewska, P. Sunderland, M. Piechota, H. Was, E. Sikora, Polyploidy formation in doxorubicin-treated cancer cells can favor escape from senescence, Neoplasia *17* (2015) 882–893, https://doi.org/10.1016/j.neo.2015.11.008.

[66] N. Noren Hooten, M.K. Evans, Techniques to Induce and Quantify Cellular Senescence, J. Vis. Exp. (2017), https://doi.org/10.3791/55533.

[67] C.A. Schmitt, B. Wang, M. Demaria, Senescence and cancer - role and therapeutic opportunities, Nat. Rev. Clin. Oncol. *19* (2022) 619–636, https://doi.org/10.1038/s41571-022-00668-4.

[68] L. Hu, H. Li, M. Zi, W. Li, J. Liu, Y. Yang, D. Zhou, Q.P. Kong, Y. Zhang, Y. He, Why senescent cells are resistant to apoptosis: an insight for senolytic development, Front Cell Dev. Biol. *10* (2022) 822816, https://doi.org/10.3389/fcell.2022.822816.

[69] A.M. Meredith, C.R. Dass, Increasing role of the cancer chemotherapeutic doxorubicin in cellular metabolism, J. Pharm. Pharm. *68* (2016) 729–741, https://doi.org/10.1111/jphp.12539.

[70] D. Stepinski, The nucleolus, an ally, and an enemy of cancer cells, Histochem. Cell Biol. *150* (2018) 607–629, https://doi.org/10.1007/s00418-018-1706-5.